

Doctoral Dissertation (Censored)

博士論文(要約)

**Organofullerene Self-assembly for
Electron Microscopy and Tomography**
(有機フラーレン集合体形成と電子顕微鏡法
および電子線トモグラフィー応用)

A Dissertation Submitted for the Degree of Doctor of Philosophy

December 2020

令和2年12月 博士(理学) 申請

Department of Chemistry, Graduate School of Science,
The University of Tokyo
東京大学大学院 理学系研究科 化学専攻

Ryosuke Sekine

関根 良輔

Abstract

This thesis describes the investigation on the preparation of amorphous fullerene assemblies and their applications in electron microscopic research. Electron microscopy is a powerful method for direct visualization of the structure of nano-size specimens, and the process of sample preparation to display the specimen under the proper environment is crucially important for the success of the TEM analysis. Amorphous fullerene assemblies such as nano-size sphere and ultra-thin film presented in the thesis help us to tune the nano environments for successful analyses by their molecular and mechanism designs.

Chapter 1 summarizes examples of structural analysis with electron microscopy, and the technical progress of sample preparation to achieve these results. Next, I shed light on the architectures of supramolecules and their potential for control of nano environments with molecular design. Soft materials are generally not robust enough under high vacuum and electron beam irradiation, which has prevented their application in electron microscopy research. To make the supramolecular concept practicable, characteristic properties of organofullerene molecules and their robust assemblies in recent studies were analyzed and used as a hint for further development.

Chapter 2 describes the method for fixing the specimens in a three-dimensional environment of the nano-size fullerene spherical assemblies. The prepared system showed excellent stability against the electron beam, and its spherical structure is suitable for structural analysis of incorporated specimens with electron tomography analysis. The generality of the specimen incorporation method to form core-shell structure is represented by its application for visualization of the spatial relationships of multiple inorganic nanoparticles or the DNA complex structures in viruses.

Chapter 6 describes the conclusion and perspectives of the developed supramolecular systems based on organofullerenes and further deduced concepts for the development of electron microscopy research.

Acknowledgement

I am very grateful to my supervisor, Prof. Eiichi Nakamura, who guided me through the process of writing this thesis. His enthusiasm, motivation, and immense knowledge helped me in not only research but also in the decision for my future.

This thesis would not be possible without the support of Dr. Koji Harano. I am very grateful for all the discussions, which were essential for understanding the experimental results, and for the guidance in the whole research process.

I also wish to express my acknowledgment to Dr. Takayuki Nakamuro for his advice and discussion both in research and life.

I also thank Dr. Rui Shang for his helpful advice, suggestions, and encouragement.

I am grateful to Dr. Prince Ravat. The turning point of my research in a positive direction was the start of collaborative work with him, and daily discussion and his supports encouraged me a lot.

I am grateful to Prof. Masahide Kikkawa and Dr. Haruaki Yanagisawa (The school of medicine) for teaching me about knowledge and techniques both on electron microscopy and structural analysis of biomaterials, strongly supporting the experiments in this thesis, and meaningful discussion.

I appreciate the support of all members from the subgroup studying electron microscopy; Mr. Toshiki Shimizu, Mr. Hiroki Hanayama, Mr. Ko Kamei, Mr. Hikaru Uchida, Mr. Dongxin Liu, Mr. Issei Tomotsuka, Mr. Keishi Takeuchi, Mr. Masaya Sakakibara, and Mr. Takato Ogata. I also thank the support from former members; Dr. Dominik Lurgerich, Dr. Junfei Xing, Dr. Chao Liu, Dr. Sai Maddala, Dr. Yuki Itabashi, Dr. Luca Schweighauser, Ms. Satori Kowashi, and Mr. Takuya Tsubota. I am especially grateful for the support of Mr. Toshiki Shimizu and Mr. Hiroki Hanayama, who spent the whole research life in the same laboratory and the same subgroup together. They have always encouraged and motivated me to continue the work in this laboratory for five years.

I am grateful to Dr. Ryuzo Tanaka (Idemitsu Kosan Co., Ltd.) and Dr. Masato Morimoto (AIST) for the meaningful discussion on the asphaltene study.

I am grateful to Prof. Motomu Tanaka and Dr. Akihisa Yamamoto (Kyoto University) for the measurement and meaningful discussion on XRR and GIWAX analysis.

I am indebted to all my laboratory colleagues who showed immense support and patience to me. I also thank Dr. Takao Kaneko, Ms. Akemi Maruyama, and Mr. Koshi Chiba, who have supported the research in this laboratory.

I would like to thank MERIT that gave me financial support and providing an opportunity to research in a global view through my Ph.D. study.

Finally, I would like to express sincere gratitude to Mr. Yusuke Sekine and Ms. Sayuri Sekine for their daily help, advice, and encouragement and their continuous love.

Table of Contents

ABSTRACT	I
ACKNOWLEDGEMENT	II
TABLE OF CONTENTS.....	IV
ABBREVIATION.....	VI
GENERAL INTRODUCTION	1
1.1 SAMPLE PREPARATION FOR DEVELOPMENT OF ELECTRON MICROSCOPY	3
1.2 SUPRAMOLECULAR CHEMISTRY FOR CONTROLLING NANO ENVIRONMENTS	5
1.3 SELF-ASSEMBLY OF ORGANOFULLERENES.....	6
1.4 THESIS OUTLINES	8
1.4 REFERENCES	9
SELF-ASSEMBLY OF ORGANOFULLERENE NANOSPHERE INCORPORATING SPECIMENS FOR ELECTRON TOMOGRAPHY ANALYSIS	11
2.1 INTRODUCTION	13
2.1.1 Preparation and application of multiple-component nano- and microspheres	13
2.1.2 Protonation-controlling molecular assembly	14
2.1.3 Characteristic structure of the organofullerenes.....	15
2.2 RESULTS AND DISCUSSION	15
2.2.1 Preparation of spherical fullerene assemblies.....	15
2.2.2 Characterization of C7H-FS	17
2.2.3 Mechanistic study of C7H-FS formation based on its preparation in different pH buffers	19
2.2.4 Injecting-speed dependency of C7H-FS size.....	20
2.2.5 Loading of fluorescent dye in C7H-FS	21
2.2.6 Loading of inorganic NPs@FS.....	23
2.2.7 Electron tomography of AuNPs@FS.....	24
2.2.8 Electron tomography of biomaterials@FS.....	28
2.3 SUMMARY	29
2.4 EXPERIMENTAL SECTION.....	30
2.4.1 General.....	30
2.4.2 Materials.....	30
2.4.3 Preparation of self-assembled particles of CnH by in-situ protonation of CnK	31
2.4.4 SEM/STEM analysis	31
2.4.5 Density measurement of C7H-FS by ultracentrifugation	32
2.4.6 Preparation of C7H-FSs in buffer solution.....	33

2.4.7 Preparation of C7H -FSs with different injection rates of water.....	33
2.4.7 TG-DTA of C7H -FS.....	35
2.4.8 DSC analysis.....	35
2.4.8 TEM and selected-area electron diffraction (SAED) analysis of C7H -FS at 25–300 °C	36
2.4.9 TEM and SAED analysis of C7H -FS at –181 °C.....	36
2.4.10 Preparation of C7H -FS incorporating fluorescent dyes.....	37
2.4.11 CLSM analysis of R6G@ C7H -FS.....	38
2.4.12 Incorporation of nanomaterials into C7H -FSs.....	38
2.4.13 Electron tomography (ET) of C7H -FS incorporating AuNPs on the edge of a holey carbon film	39
2.4.14 ET of C7H -FS incorporating AuNPs on continuous carbon film.....	41
2.4.15 ET of C7H -FS incorporating biomolecules on continuous carbon film	44
2.5 REFERENCES	47
第3章 本章については、5年以内に特許申請するため、非公開.....	49
第4章 本章については、5年以内に特許申請するため、非公開.....	51
第5章 本章については、5年以内に特許申請するため、非公開.....	53
CONCLUSION AND PERSPECTIVES	55

Abbreviation

2D	two-dimensional	LS	Laurylsulfobetaine
3D	three-dimensional	MD	molecular dynamics
aC	amorphous carbon	MM	molecular mechanics
AFM	atomic force microscopy (microscope)	m.p.	melting point
aq	aqueous solution	NMR	nuclear magnetic resonance
a.u.	arbitrary unit	OM	optical microscopy
AuNP	gold nanoparticle	PBS	phosphate-buffered saline
BP	bandpass	PEG	polyethyleneglycol
C.A.	contact angle	PEI	polyethyleneimine
CAC	critical aggregation concentration	<i>Pow</i>	partition coefficients between 1-octanol and water
CHAPS	3-[(3-Cholamidopropyl)dimethylamm onio]-1-propanesulfonate	PSS	poly(styrenesulfonate)
CLSM	confocal laser scanning microscopy	QD	quantum dot
CMC	critical micellar concentration	SA	sulfonic acid
Cryo	cryogenic	SAED	selected area electron diffraction
CVD	chemical vapor deposition	SAM	self-assembled monolayer
DLS	dynamic light scattering	SAXS	small-angle X-ray scattering
DMF	<i>N,N</i> -dimethylformamide	SB	sulfobetaine
DSC	differential scanning calorimetry	SEM	scanning electron microscopy (microscope)
eq.	equivalent	SLD	scattering length density
ED	electron diffraction	SNR	signal-to-noise ratio
EM	electron microscopy	STEM	scanning transmission electron microscopy (microscope)
ET	electron tomography	TEM	transmission electron microscopy (microscope)
FFT	fast Fourier transform	TG-DTA	thermogravimetry-differential thermal analysis
FS	fullerene spherical assembly (fullersphere)	THF	tetrahydrofuran
GIWAX	grazing-incidence wide-angle X- ray scattering	Tris	tris(hydroxymethyl)- aminomethane
GLC	graphene liquid cell	UV	ultraviolet
HPLC	high pressure (performance) liquid chromatography	Vis	visible
ICP-AES	inductively coupled plasma atomic emission spectroscopy	XRD	X-ray diffraction
		XRR	X-ray reflectivity
		γ -CD	γ -cyclodextrin

Chapter 1.

General Introduction

Chapter 1

1.1 Sample preparation for development of electron microscopy

Structural analysis of nanosized objects is an essential technology in a variety of fields in science and technology to understand their structure-function relationships. While spectroscopic analysis provides the average information of numerous numbers of specimens in the bulk, electron microscopy allows us to study static and dynamic structures of individual objects at the nanoscale. Among various microscopic methods, electron microscopy (EM) is a powerful and versatile analytical tool for imaging specimens with high spatial resolution in three-dimensional spaces^{1,2,3}. In EM imaging, specimen preparation should be taken special care to visualize the inherent structure of individual nanomaterials without deformation or aggregation during sample preparation⁴.

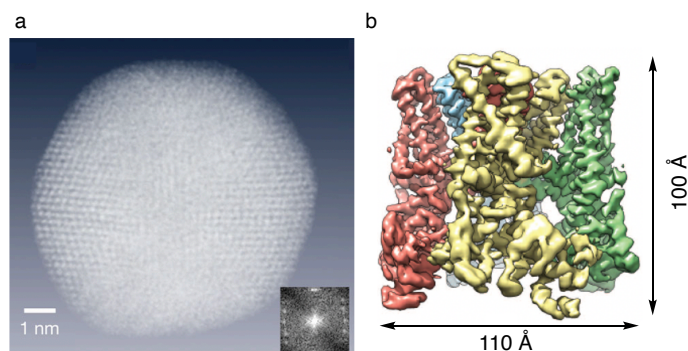


Figure 1.1. Reconstructed three dimensional structures with EM. (a) A gold nanoparticle (10 nm). Adapted with permission from ref. 2. Copyright 2012 Springer Nature. (b) A membrane protein TRPV1. Adapted with permission from ref. 3. Copyright 2013 Springer Nature.

For the most of nanoparticles, drop-casting is the first choice to prepare their samples on EM grids with continuous support films such as amorphous carbon or silicon dioxide. In this method, the background contrasts arise only from the thin support film, and specimen structures can be obtained with high image contrasts. However, the process manipulating dispersions of the nanosized specimens in a liquid phase often suffer from their agglomeration represented by coffee-ring effect⁵ or denaturation during drying processes⁶. To avoid the sample agglomeration, various methods have been developed such as adding surfactants to stabilize the dispersed states⁵ or nebulizing the dispersion to reduce the liquid droplet size for isolating individual structures¹.

There are two major techniques to maintain the specimen structure without the undesirable deformation during drying process, instead of the drop-cast method. One is a liquid-cell TEM in which the specimen dispersion is sandwiched and held by two thin films such as monolayer graphenes⁷ or silicon membrane⁸. The method is also beneficial to observe the dynamics of incorporated specimens in liquid^{9,10}, while its application is limited for only specimens with high crystallinity or high contrasts due to relatively thick

supporting materials (containing films and liquids) and their movements inhibiting super imposition of neighboring image frames.

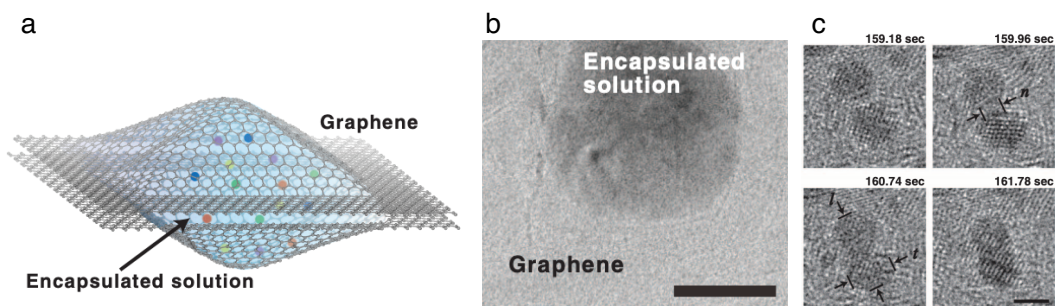


Figure 1.2. A liquid cell encapsulating specimens in their dissolved or dispersed states. (a) A schematic illustration of a graphene liquid cell (GLC). (b) TEM image of a GLC. (c) Snapshots of a coalescence behavior of Pt nanocrystals. Scale bars: 50 nm for b. 2 nm for c. All images in this figure are reprinted with permission from ref. 9. Copyright 2013 American Association for the Advancement of Science.

The other method is a cryo-electron microscopy in which the hydrated (solvated) specimens are fixed in vitreous ice by plunge freezing their dispersions at cryogenic temperatures^{11,12}. The method is widely applied for imaging biomolecules, and single-particle-analysis, a 3D reconstruction technique, enable us to build atomic models made from light elements without their crystals^{13,14}. While it can prevent the most of undesirable denaturation of specimens in an ideal condition, it still requires the optimization of preparation conditions¹⁵.

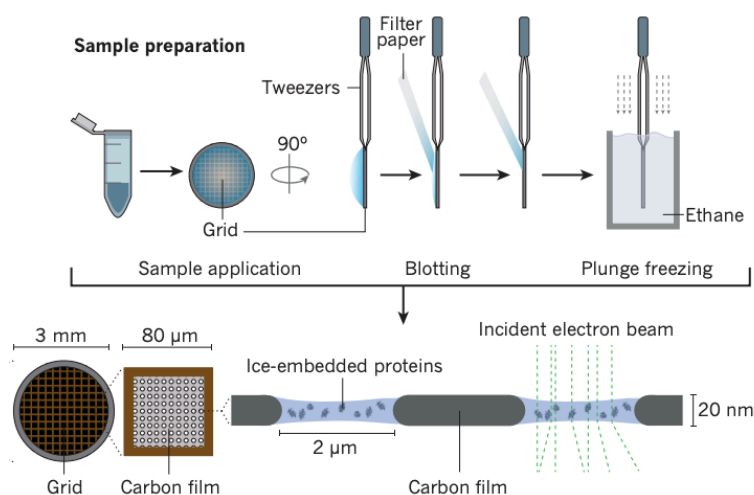


Figure 1.3. A preparation scheme of specimens in vitreous ice for cryo-EM observation. Adapted with permission from ref.12. Copyright 2016 Springer Nature.

1.2 Supramolecular chemistry for controlling nano environments

Supramolecular chemistry has a wide potential for improving sample preparation of EM due to its controllability of nano environments, while the methods described in a previous section have been developed mainly on nanotechnology. Thus, I discuss the key feature of supramolecules likely being useful for EM research, that is the ability to control the specimen location by their higher-order structures and protect the specimen structure from outer environments. For example, the supramolecules with their repeated structures have been utilized as templates to form various nanosized architectures such as protein arrays¹⁶ or colloidal assemblies showing optical active properties¹⁷. This technique could be utilized for displaying specimens in TEM images in its appropriate density or capturing the targeted structures selectively from crude mixtures.

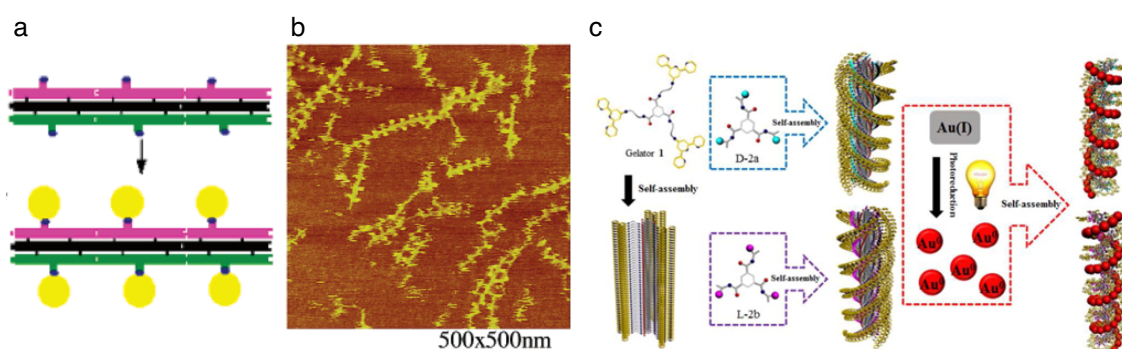


Figure 1.4. Nanosized architectures utilizing self-assemblies as templates. (a) Proteins on self-assembly of DNAs. Adapted with permission from ref. 16. Copyright 2004 American Chemical Society. (b) AuNPs on self-assembly of chiral nanofibers. Adapted with permission from ref. 17. Copyright 2014 American Chemical Society.

Self-assembled monolayer (SAM) is applied for coating nanoparticle surface^{18,19}. It stabilizes the dispersed state of nanoparticle by adding charge and preventing the contact of nanoparticle surface with neighboring nanoparticles. Reverse micelle is utilized for transporting biomolecules in organic phase without denaturation. The reverse micelle structure maintains the water droplets stably and the polar head groups of surfactants prevent the collision or exposure of incorporated molecules to oil phase²⁰.

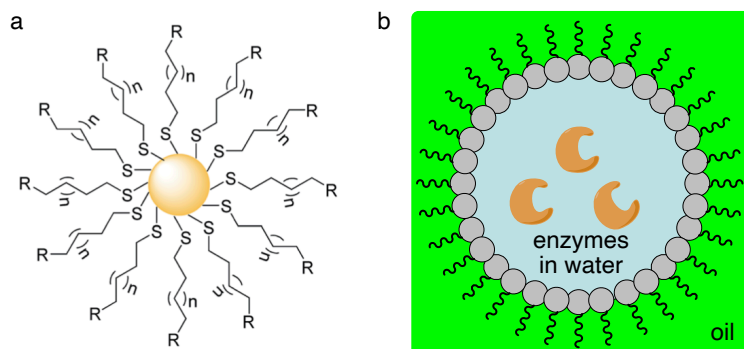
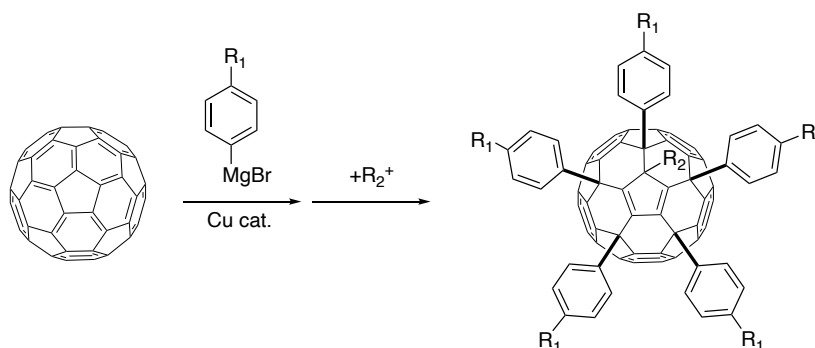


Figure 1.5. Protection of various nanomaterials with self-assemblies. (a) AuNPs functionalized with SAM. Adapted with permission from ref. 19. Copyright 2016 The Royal Society of Chemistry. (b) Enzymes incorporated in water droplets stabilized by reverse micelle.

Some of those supramolecular approaches have been utilized for sample preparation of EM, by coupling with other supporting materials in drop cast methods⁵ or cryo-EM methods²¹. However, their applications as a main skeleton of supporting material having self-standing or rigid property were limited in few examples²² because of following two problems. One is their structural flexibility based on noncovalent bonding which prevents the forming of rigid structure and induces structural change depending on surrounding environments. The other is its instability under electron beam irradiation such as phase transition of crystalline domains.

1.3 Self-assembly of organofullerenes

Our group has developed the synthetic method of organofullerenes through penta-addition reaction on C₆₀²³. Various substituents can be introduced through the reactions, and their post-modified molecules can act as amphiphiles^{24,25,26,27}, since the reactions occur at hemisphere of C₆₀ selectively to generate anisotropy.



Scheme 1.1. Penta-addition reaction of C₆₀ molecule.

The diversity of synthesized fullerene derivatives has enabled us to construct various supramolecular architectures. (4-carboxylphenyl) $_5$ C $_{60}$ CH $_3$ can favorably interact with the metal oxide surface and form SAM applied as photoactive acceptor of electronic devices²⁸. Potassium salts of (4-alkylphenyl) $_5$ C $_{60}$ H spontaneously form bilayer vesicles through injection of the solution in THF to water²⁶. The original (4-alkylphenyl) $_5$ C $_{60}$ H also have an amphiphilic property in terms of aliphatic/aromaticity²⁹. These supramolecules have rigid structures both in ambient condition and high vacuum, and their structure are observable in electron microscopic condition without polymerization nor conductive coating.

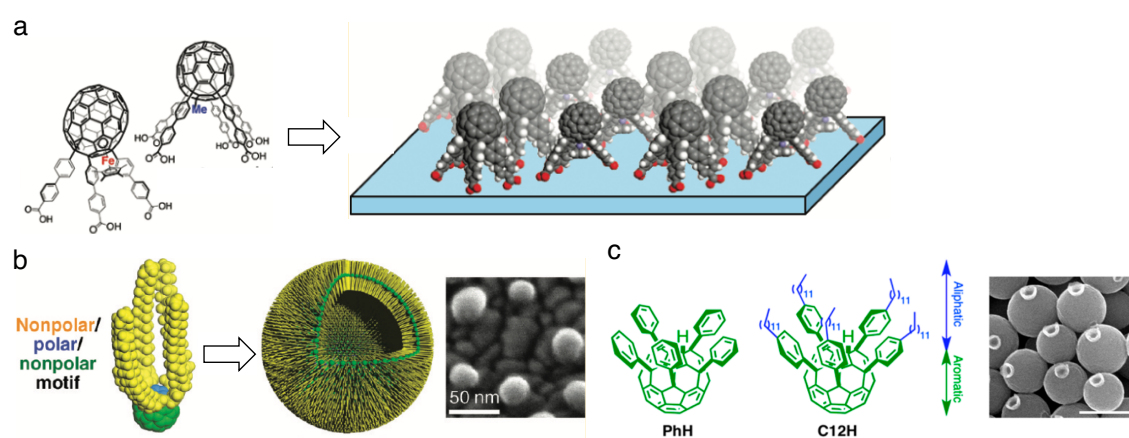


Figure 1.6. Supramolecular architectures of organofullerenes. (a) SAM of (4-carboxylphenyl) $_5$ C $_{60}$ CH $_3$ on ITO substrate. Adapted with permission from ref. 28. Copyright 2011 American Chemical Society. (b) Bilayer vesicle made of potassium salt of (4-alkylphenyl) $_5$ C $_{60}$ H. Adapted with permission from ref. 26. Copyright 2011 American Chemical Society. (c) Anisotropic amorphous particle made of (4-alkylphenyl) $_5$ C $_{60}$ H. Adapted with permission from ref. 29. Copyright 2016 American Chemical Society.

The excellent stability of fullerene assemblies under electron beam irradiation is the reason I focused on them for EM application among various supramolecules. Especially, the bilayer of fluorous-fullerene amphiphile can retain an incorporated water droplet without any decomposition in a high vacuum at an electron dose of 10^6 e $^-$ nm $^{-2}$ in total³⁰. The stability would likely come from a C $_{60}$ skeleton, that are stable for multiple charge accumulations³¹, and its main body is shared with all organofullerenes. Thus, the various architectures made from organofullerenes are expected to pioneer the application of supramolecules controlling nano environments in electron microscopy.

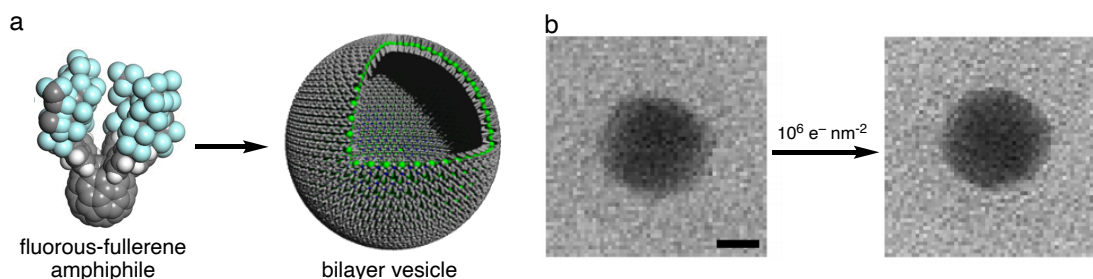


Figure 1.7. Stable vesicle structure in a (S)TEM observation condition. (a) A model of a bilayer vesicle made of potassium salt of fluoroalkyl-substituted fullerenes. (b) STEM images of the vesicle containing water inside under a constant irradiation of electron beam till $10^6 \text{ e}^- \text{ nm}^{-2}$. Adapted with permission from ref. 29. Copyright 2018 American Chemical Society.

1.4 Thesis outlines

To demonstrate the potential of supramolecules in solving the conventional problems in EM, I have investigated the preparation of amorphous fullerene assemblies and their applications as supporting material for structural analyses of nanoobjects from inorganic nanoparticles to proteins with EM in my doctoral course study.

In chapter 2, a preparation method and applications of organofullerene a nano- or microsphere made of (4-alkylphenyl) $_5\text{C}_{60}\text{H}$ is described. The assembly is prepared through an antisolvent injection against the fullerene in an organic solvent. It can incorporate various samples such as inorganic nanoparticles and biomolecules from their solutions in a buffer by using a potassium salt of (4-alkylphenyl) $_5\text{C}_{60}\text{H}$ as starting material. Since the constituent fullerene layer is robust enough to fix the 3D structures of incorporated nanomaterials while being amorphous and low density, it is useful as a supporting material for EM observation at a wide temperature range. The application during analyzing the relative positions of multiple gold nanoparticles in fullerene nanospheres demonstrated the advantage of its spherical shape for improving 3D data collection of incorporated nanoobjects.

Through these investigations, the advantage of using supramolecules for EM research, that is their controllability of nano environments, was demonstrated in several aspects such as control of specimen locations/orientations in nanoscale and a fixation/protection of their structures from outer environments.

1.4 References

- 1) Hinman, J. G.; Hinman, J. J.; Janicek, B. E.; Huang, P. Y.; Suslick, K. S. Murphy C. J. Ultrasonic Nebulization for TEM Sample Preparation on Single-Layer Graphene Grids. *Nano Lett.* **2019**, *19*, 1938–1943.
- 2) Scott, M.; Chen, C. C.; Mecklenburg, M. *et al.* Electron tomography at 2.4-ångström resolution. *Nature* **2012**, *483*, 444–447.
- 3) Liao, M.; Cao, E.; Julius, D. *et al.* Structure of the TRPV1 ion channel determined by electron cryo-microscopy. *Nature* **2013**, *504*, 107–112.
- 4) Chen, Q.; Dwyer, C.; Sheng, G.; Zhu, C.; Li, X.; Zheng, C.; Zhu, Y. Imaging Beam-Sensitive Materials by Electron Microscopy. *Adv. Mater.* **2020**, *32*, 1907619.
- 5) Michen, B.; Geers, C.; Vanhecke, D.; Endes, C.; Rothen-Rutishauser.; Balog, S.; Petri-Fink, A. Avoiding drying-artifacts in transmission electron microscopy: Characterizing the size and colloidal state of nanoparticles. *Sci. Rep.* **2015**, *5*, 9793.
- 6) Tsuda, T.; Nemoto, N.; Kawakami, K.; Mochizuki, E.; Kishida, S.; Tajiri, T.; Kushibiki, T.; Kuwabata, S. SEM observation of wet biological specimens pretreated with room-temperature ionic liquid. *ChemBioChem.* **2011**, *12*, 2547–255
- 7) Textor, M.; De Jonge, N. Strategies for Preparing Graphene Liquid Cells for Transmission Electron Microscopy. *Nano Lett.* **2018**, *18*, 3313–3321.
- 8) Mirsaidov, U. M.; Zheng, H.; Casana, Y.; Matsudaira, P. Imaging Protein Structure in Water at 2.7 nm Resolution by Transmission Electron Microscopy. *Biophysical J.* **2012**, *102*, L15–L17.
- 9) Yuk, J. M.; Park, J.; Ercius, P.; Kim, K.; Hellebusch, D. J.; Crommie, M. F.; Lee, J. Y.; Zettl, A.; Alivisatos, A. P. *Science* **2012**, *336* (6077), 61–64.
- 10) Zhu, C., Liang, S., Song, E. *et al.* In-situ liquid cell transmission electron microscopy investigation on oriented attachment of gold nanoparticles. *Nat. Commun.* **2018**, *9*, 421.
- 11) Dubochet, J.; Adrian, M.; Chang, J. J.; Homo, J. C.; Lepault, J.; McDowell, A. W.; *et al.* Cryo-Electron Microscopy of Vitrified Specimens. *Q. Rev. Biophys.* **1988**, *21*, 129–228.
- 12) Fernandez-Leiro, R.; Scheres, S. Unravelling biological macromolecules with cryo-electron microscopy. *Nature* **2016**, *537*, 339–346.
- 13) Yip, K. M.; Fischer, N.; Paknia, E. *et al.* Atomic-resolution protein structure determination by cryo-EM. *Nature* **2020**, *587*, 157–161.
- 14) Nakane, T.; Kotecha, A.; Sente, A. *et al.* Single-particle cryo-EM at atomic resolution. *Nature* **2020**, *587*, 152–156.
- 15) Glaeser, M. Proteins, interfaces, and cryo-EM grids, *Curr. Opin. Colloid Interface Sci.* **2018**, *34*, 1–8.
- 16) Li, H.; Park, S. H.; Reif, J. H.; LaBean, T. H.; Yan, H. DNA-Templated Self-Assembly of Protein and Nanoparticle Linear Arrays. *J. Am. Chem. Soc.* **2004**, *126*, 418–419.
- 17) Jung, S. H.; Jeon, J.; Kim, H.; Jaworski, J.; Jung, J. H. Chiral arrangement of achiral Au nanoparticles by supramolecular assembly of helical nanofiber templates. *J. Am. Chem. Soc.* **2014**, *136*, 6446–6452.

- 18) Love, J. C.; Estroff, L.A.; Kriebel, J. K.; *et al.* Self-Assembled Monolayers of Thiolates on Metals as a Form of Nanotechnology. *Chem. Rev.* **2005**, *105*, 1103–1170.
- 19) Jadhav, S. A. Functional self-assembled monolayers (SAMs) of organic compounds on gold nanoparticles. *J. Mater. Chem.*, **2012**, *22*, 5894–5899.
- 20) Abetxuko, A. R.; deAlcázar, D. S.; Muñumer, P. Tunable Polymeric Scaffolds for Enzyme Immobilization. *Front. Bioneng. Biotechnol.* **2020**, *8*, 830.
- 21) Meyerson, J.; Rao, P.; Kumar, J. *et al.* Self-assembled monolayers improve protein distribution on holey carbon cryo-EM supports. *Sci. Rep.* **2014**, *4*, 7084.
- 22) Wang, L. G.; Ounjai, P.; Sigworth, F. J. Streptavidin crystals as nanostructured supports and image-calibration references for cryo-EM data collection. *J Struct Biol* **2008**, *164*, 190–198.
- 23) Sawamura, M.; Iikura, H.; Nakamura, E. The First Pentahaptofullerene Metal Complexes. *J. Am. Chem. Soc.* **1996**, *118*, 12850–12851.
- 24) Zhou, S.; Burger, C.; Chu, B.; Sawamura, M.; Nagahama, N.; Toganoh, M.; Hackler, U. E.; Isobe, H.; Nakamura, E. Spherical Bilayer Vesicles of Fullerene Based Surfactants in Water: A Laser Light Scattering Study. *Science* **2001**, *291*, 1944–1947.
- 25) Matsuo, Y.; Kanaizuka, K.; Matsuo, K.; Zhong, Y.-W.; Nakae, T.; Nakamura, E. Photocurrent-Generating Properties of Organometallic Fullerene Molecules on an Electrode, *J. Am. Chem. Soc.* **2008**, *130*, 5016–5017.
- 26) Homma, T.; Harano, K.; Isobe, H.; Nakamura, E. Preparation and Properties of Vesicles Made of Nonpolar/Polar/Nonpolar Fullerene Amphiphiles. *J. Am. Chem. Soc.* **2011**, *133*, 6364–6370.
- 27) Nitta, H.; Harano, K.; Isomura, M.; Backus, E. H. G.; Bonn, M.; Nakamura, E. Conical Ionic Amphiphiles Endowed with Micellization Ability but Lacking Air-Water and Oil-Water Interfacial Activity. *J. Am. Chem. Soc.* **2017**, *139*, 7677–7680.
- 28) Matsuo, Y.; Ichiki, T.; Nakamura, E. Molecular Photoelectric Switch Using a Mixed SAM of Organic[60]Fullerene and [70]Fullerene Doped with a Single Iron Atom. *J. Am. Chem. Soc.* **2011**, *133*, 9932–9937.
- 29) Baire, P.; Minami, K.; Hill, J. P.; Nakanishi, W.; Shrestha, L. K.; Liu, C.; Harano, K.; Nakamura, E.; Ariga, K. Supramolecular Differentiation for Construction of Anisotropic Fullerene Nanostructures by Time-Programmed Control of Interfacial Growth. *ACS Nano* **2016**, *10*, 8796–8802.
- 30) Abuillan, W.; Becker, A. S.; Demé, B.; Homma, T.; Isobe, H.; Harano, K.; Nakamura, E.; Tanaka, M. Neutron Scattering Reveals Water Confined in a Watertight Bilayer Vesicle. *J. Am. Chem. Soc.* **2018**, *140*, 11261–11266.
- 31) Matsuo, Y.; Nakamura, E. Syntheses, Structure, and Derivatization of Potassium Complexes of Penta(organo)[60]fullerene-Monoanion, -Dianion, and -Trianion into Hepta- and Octa(organo)fullerenes. *J. Am. Chem. Soc.* **2005**, *127*, 8457–8466.

Chapter 2.

Self-assembly of organofullerene nanosphere incorporating specimens for electron tomography analysis

This chapter was published in the following paper and reproduced with the permission from 2021, American Chemical Society.

Ryosuke Sekine, Prince Ravat, Haruaki Yanagisawa, Chao Liu, Masahide Kikkawa, Koji Harano, Eiichi Nakamura “Nano- and Microspheres Containing Inorganic and Biological Nanoparticles: Self-Assembly and Electron Tomographic Analysis”, *J. Am. Chem. Soc.* **2021**, <https://doi.org/10.1021/jacs.0c11944>

Chapter 2

2.1 Introduction

2.1.1 Preparation and application of multiple-component nano- and microspheres

Multiple-component nano- and microspheres containing various nanoparticles represented by core-shell particles are studied and applied in various fields such as optoelectronics and medicines^{1,2}. The advantage of using the architecture is producing the superior physical and chemical properties of incorporated nanoparticles compared with those in their dispersed/dried states. These incorporated particles could be protected from outer environment³, fixed in their isolated/dispersed states⁴, and given new functions through interaction between multiple component⁵. While organic/inorganic core/shell structures have a great research interest as described before among the various multiple-component systems¹, the most of systems are constructed by polymer systems, and the applicable range of specimens to be incorporated would be limited. For example, the emulsion polymerization required the sequence of seeding, emulsification of monomer with surfactants, and polymerization processes⁶, that are only applicable for chemically/mechanically stable inorganic nanoparticles. Thus, to develop a non-polymer method applicable for various specimens, I focused on a hydrophobic molecular assembly prepared through anti-solvent injection that is a method to form nano/sub-micron organic spheres with a simple step (Figure 2.1a)⁷. However, the method also has a problem to be solved for preparing multiple-component nano- and micro-spheres. Since the assembly was produced through the nucleation and growth steps typically with water as an anti-solvent, it was affected with ionic strength of aqueous phase often resulting a salting out, and nanoparticles/structures dispersed in buffers looked difficult to be incorporated inside.

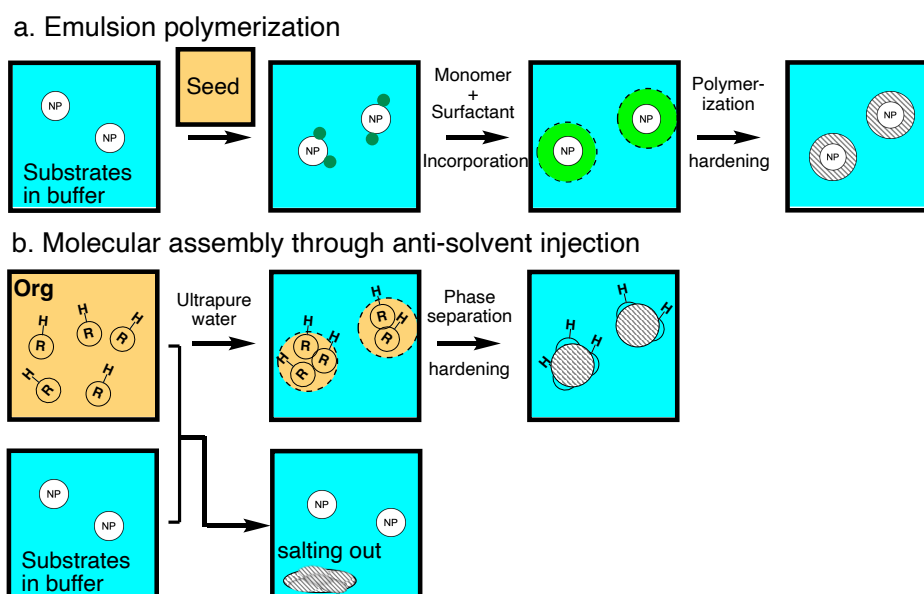


Figure 2.1. Schematic illustration to produce core-shell particles. (a) Emulsion polymerization. (b) The alternative hydrophobic molecular assembly method with its current problem to be solved.

Chapter 2

2.1.2 Protonation-controlling molecular assembly

To prepare multiple-component nano- and micro-spheres through hydrophobic molecular assemblies without salting-out, I planned the strategy of using a transient polar molecule as a starting material such as an anion species to be protonated. In the system, the anion adjusted its acidity properly would be able to exist stably even after mixing with substrates in a buffer, and gradual protonation producing the neutral species would initiate nucleation of the assemblies (Figure 2.2a). Since the rate of nucleation and growth steps in the procedure will become milder than that in a system using a neutral species, the multiple-component nano- and micro-spheres can suppress the salting-out effect. For this purpose, I focused on pentaarylated [60]fullerenes bearing five alkyl groups (**CnH**)⁸. The molecules are originally hydrophobic, on the other hand, it can exist as a hydrophilic anion species (**CnK**) in water because its negative charge on a cyclopentadiene part is stabilized by a π -conjugated C₅₀ skeleton (unreacted parts in C₆₀ molecule through the penta-addition reaction) and its pK_a value is estimated to be lower than 13 (Figure 2.2b)⁹.

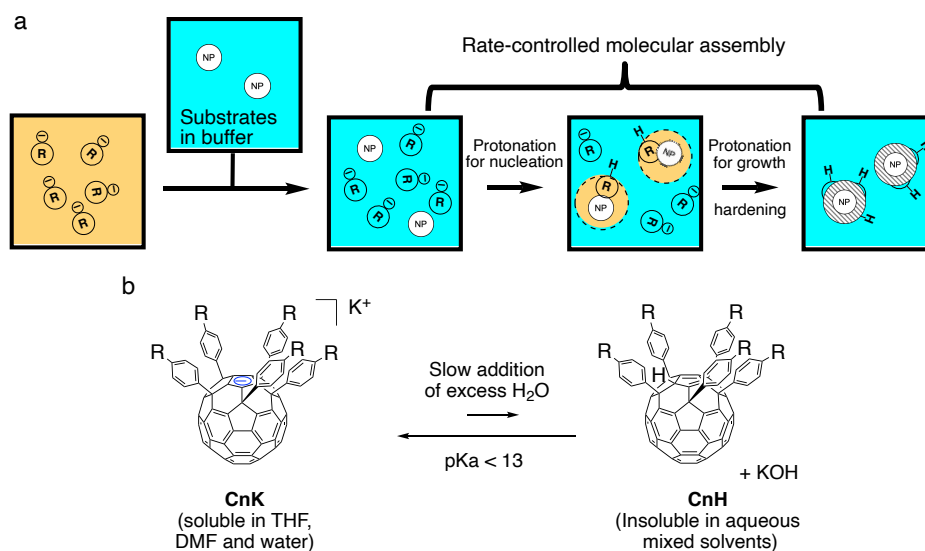


Figure 2.2. A preparation method of multiple-component nano- and micro-spheres by a protonation-controlling molecular assembly. (a) Schematic illustration of the improved process of hydrophobic assembly. (b) An equilibrium of pentaarylated [60]fullerene between its neutral species and its anion species.

Chapter 2

2.1.3 Characteristic structure of the organofullerenes

The other properties of **C_nH** are also suitable for preparing multiple-component nano- and microspheres. A shell substrate of the multiple-component spheres is required to have an affinity with nanomaterials to be incorporated and an amorphous property to mix with nanoparticles efficiently. **C_nH** can be functionalized with various substituents to tune its solubility^{10, 11}, crystallinity, and introduce chemical interaction manners adjusted for target specimens^{12, 13, 14}.

Besides, its pseudo *C*₅ symmetry, adaptable its enhancement by the introduction of large substituents, contributes to suppressing its crystallinity (Figure 2.3).

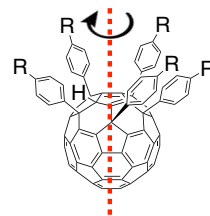


Figure 2.3. A pseudo *C*₅ axis on **C_nH**.

It should be noted here that the preparation of fullerene nanospheres containing biological materials in Section 2.2.8 was done collaboratively with my-coworker Dr. Ravat and I'm very grateful for his help. The electron tomography analysis and other works in Sections 2.2.7–8, 2.4.5, 2.4.7, and 2.4.13–15 were done collaboratively with my-coworkers Prof. Kikkawa and Dr. Yanagisawa, and I'm very grateful for their supports.

2.2 Results and discussion

2.2.1 Preparation of spherical fullerene assemblies

I chose five fullerene compounds (**C_nH**, *n* = 0, 1, 7, and 13) for preparing a fullerene spherical assembly (fullersphere, FS) a shell part of the multiple-component spheres. **C₀H** has a strong crystalline property. **C₁H** has methyl groups potentially inhibiting the stack of molecules with vertical direction by steric repulsion. This steric factor and the effect of suppressing its crystallinity due to pseudo *C*₅ symmetry are increased with the order of **C₁H**, **C₇H**, **C₁₃H**. In a typical procedure to prepare a fullerene assembly, **C_nH** (6.3 μmol) was dissolved to THF (0.8 mL) and deprotonated by *t*-BuOK (1.5 equiv, 1 M in THF) to prepare **C_nK** solution. Then ultrapure water (4.2 mL) was injected into the solution (0.16 mL/min) through a syringe with continuous stirring (500 rpm) at 25 °C, and orange-colored suspensions were obtained (Figure 2.4a). DLS analysis of the suspensions showed the peak diameter of 100 nm to 1 μm depends on the substrates (Figure 2.4b).

Chapter 2

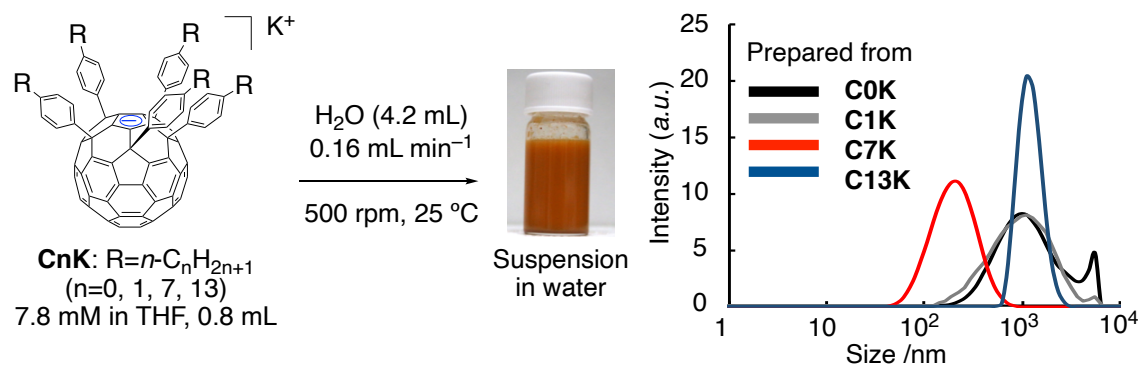


Figure 2.4. Formation of micro-assembly prepared from **CnK**. (a) A typical procedure to obtain a suspension of micro-assembly. (b) DLS data for the suspensions prepared from **CnK** are shown as intensity-weighted size distribution.

The suspension was diluted with 45 mL of water and centrifuged portion wise to collect the fullerene assembly as an orange solid. SEM analysis of the assembly revealed that the morphology of the solid largely differs among the compounds investigated (Figures 2.5a). The assembly prepared from **C7K** shows its spherical structure with a uniformly smooth surface (Figure 2.5d), whereas the assembly prepared from no alkyl (**C0K**) or methyl groups (**C1K**) resulted in crystalline precipitate (Figures 2.5b-c). The assembly prepared from a molecule with long alkyl chains (**C13K**) also shows its spherical structure, but the assembly tends to stick to each other due to the softness of the self-assembled structures (Figure 2.5e). Through the above structural characterization, the FS prepared from **C7K** was selected as the best component to construct a shell part of the multiple-component spheres.

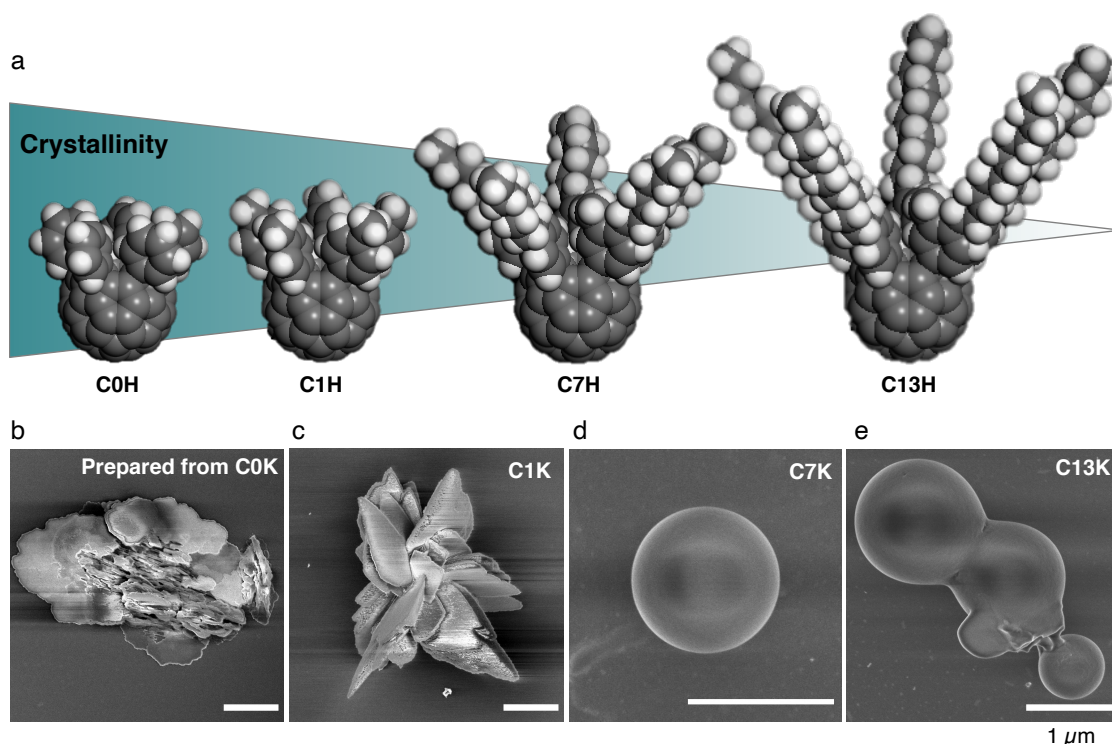


Figure 2.5. The morphologies of fullerene assemblies prepared from **CnK**. (a) Molecular structures of **CnHs** as protonated forms of **CnKs**. (b) STEM image of a fullerene assembly prepared from **C0K**. (c) That prepared from **C1K**. (d) That prepared from **C7K**. (e) That prepared from **C13K**. Scale bars: 1 μm .

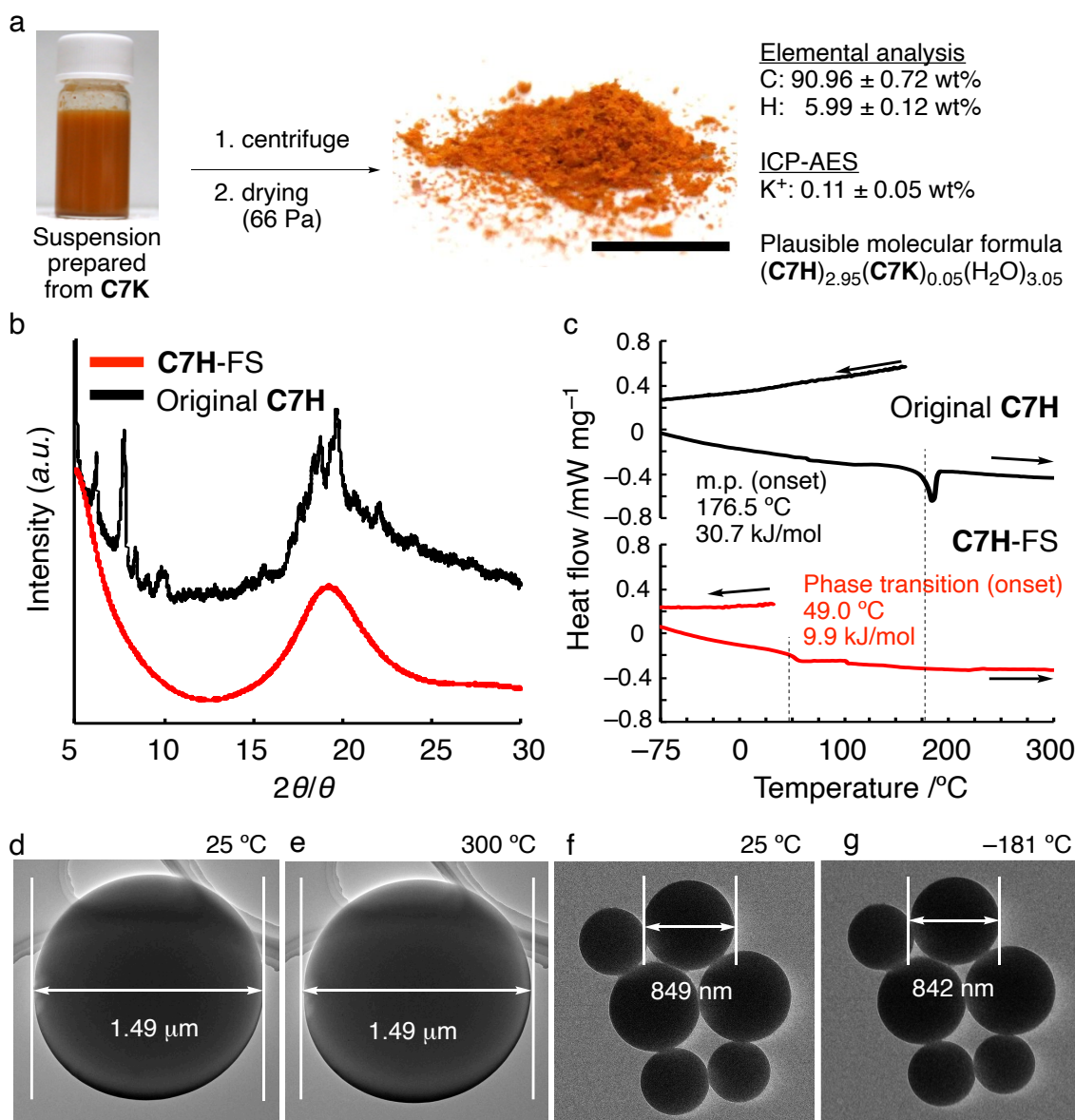
2.2.2 Characterization of **C7H-FS**

The FS prepared from **C7K** was also prepared on a larger scale starting from 20.0 mg of **C7H** to obtain 16.1 mg as orange-colored powder, which was used for further characterization. Using the isolated powder, the molecular composition of the FS was assigned to be $(\text{C7H})_{0.95}(\text{C7K})_{0.05}(\text{H}_2\text{O})_{3.05}$ through ICP-AES and elemental analysis (Figure 2.6a). As the specific experimental procedures, ICP analysis was conducted on a sample solution prepared by oxidation decomposition of FS with $\text{HNO}_3/\text{H}_2\text{SO}_4$ and dilution by ultrapure water. The prepared solution assignable to be 0.200 mg/mL of the FS showed $2.23 \pm 0.97 \times 10^{-4}$ mg/mL of K^+ existence, which corresponds to 4.66% of **C7H**. The element weight ratio of dried powder was determined to be 90.96 ± 0.72 wt% for carbon, 5.99 ± 0.12 wt% for hydrogen respectively. Since no other element was observed in the above analyses, the remaining 3.05 wt% was attributed to oxygen. The result reflects the existence of 3 water molecules coordinating on a single **C7H** molecule.

Bulk and microscopic structural characterization of the **C7H-FS** proved that its homogeneously amorphous structure suitable for incorporating nano-size specimens inside. The XRD pattern of a powder form of the **C7H-FS** shows no periodic pattern in contrast to the as-prepared crystalline **C7H** powder (Figure 2.6b). Differential scanning

Chapter 2

calorimetry analysis indicates thermal stability of **C7H-FS** up to 300 °C where its weight loss starts in thermogravimetric analysis except for a small endothermic peak at 49 °C, while the as-prepared crystalline **C7H** has a melting point at 176.5 °C with a large endothermic peak (Figure 2.6c). The cooling process of **C7H-FS** neither indicates no phase transition till –75 °C. TEM images and selected area electron diffractions also support that the individual particle of **C7H-FS** does not have a crystalline property at 25 °C and –181 °C (see Figures S2.4 and S2.5 in SI). The **C7H-FS** particle could maintain its smooth spherical structure without a change in the particle size upon heating to 300 °C and cooling to –181 °C (Figures 2.6d-g). These results suggest the stable amorphous phase in a wide temperature range useful for its various application as multiple-component spheres.



Chapter 2

Figure 2.6. Characterization of **C7H-FS**. (a) Preparation of a powder of **C7H-FS** and assignment of its elemental ratio. (b) Powder XRD of **C7H** (black line) and **C7H-FS** (red). (c) DSC chart on **C7H** powder (black) showing melting at 176.5 °C, and bulk **C7H-FS** (red) showing a minor endothermic peak at 49.0 °C. (d, e) TEM images of **C7H-FS** with the diameter maintained during the heating process up to 300°C. (f, g) TEM images of **C7H-FS** with the diameter maintained during the cooling process to -181 °C.

2.2.3 Mechanistic study of **C7H-FS** formation based on its preparation in different pH buffers

To prove the role of an equilibrium between **CnH** and **CnK** for a formation of **C7H-FS** in water, **C7H-FS** is prepared with different pH buffers as anti-solvents. Glycylglycine-piperazine dichloride buffers (10 mM), which can be prepared in wider pH ranges than typical buffer systems, are used for demonstration. 4.2 mL of the prepared buffers (pH 5.05-9.05) were injected to 0.8 mL of **C7K** solutions (7.8 mM, 10.0 mg) in THF with syringe pump (injection rate 0.16 mL/min) at 25 °C (Figure 2.7a). At first, the buffers effects were monitored with the yield of **C7H-FS** that are ratios of stable suspended fractions against non-structural precipitations (Figure 2.7b). Although all substrates were precipitated immediately in pH 5.05 condition, other conditions over pH 5.50 afford **C7H-FS** formation. The yield increased by use of higher pH buffer and reached up to $86 \pm 5\%$ at the injection of pH 9.05 buffer. The precipitation in the low pH region is a result that the protonation on **C7K** is too quick to form stable nano- or micro-size solid colloids. Besides, the behavior of **C7H-FS** yield in higher pH region can be interpreted that the rate of **C7H** formation is controlled well by maintain the equilibrium favoring **C7K**. The other analysis based on the average size with DLS measurement was conducted after the solvent of suspension was exchanged to ultrapure water by repetition of centrifugation and refill of ultrapure water (Figure 2.7c). As a result, I found the slight size increase corresponding to pH increase. The behavior also indicates the nucleation of **C7H-FS** is suppressed by maintaining the equilibrium favoring **C7K** and the individual particles can grow larger. Besides, it is proved that the core shell **C7H-FS** formation can be applied by incorporating nanomaterials from various solvated systems, since it can form in a wide pH range stably.

Chapter 2

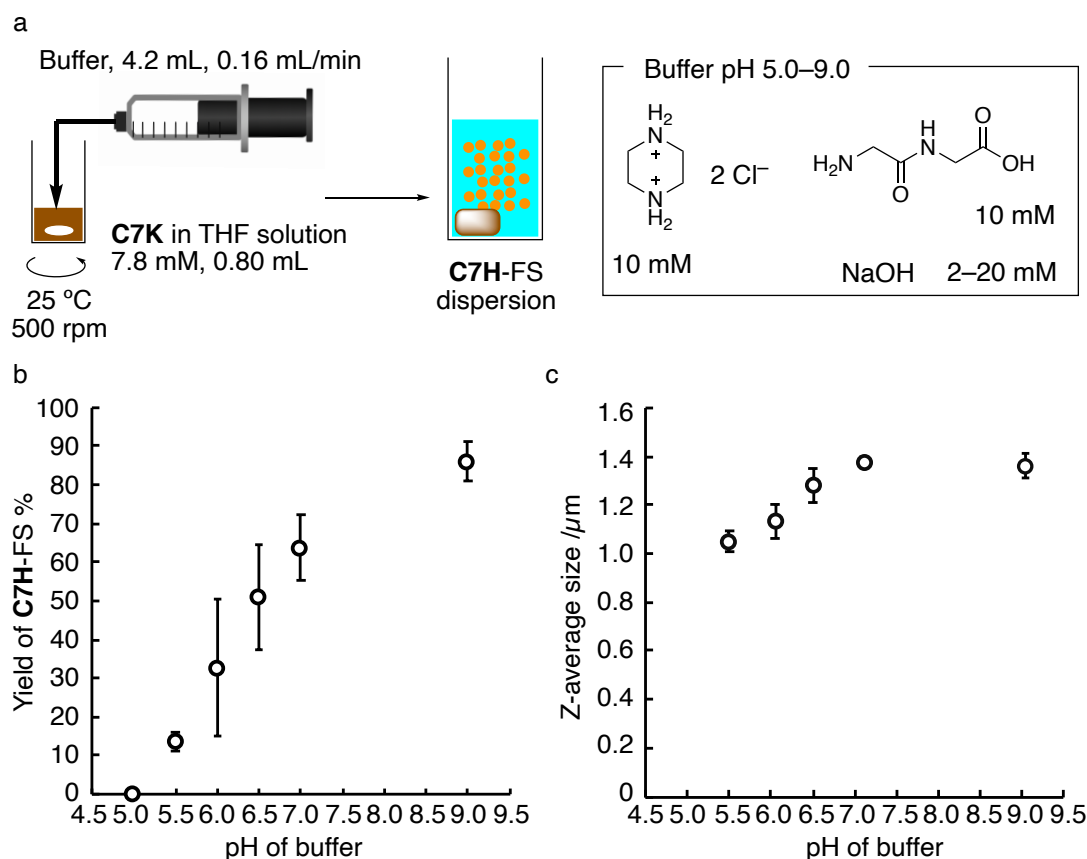


Figure 2.7. **C7H-FS** preparation in different pH buffers. (a) An experimental setup of **C7H-FS** preparation. (b) Dependence of **C7H-FS** yield on pH of glycylglycine–piperazine dichloride buffer (10 mM). (b) Dependence of diameter of FS (DLS) on buffer pH.

2.2.4 Injecting-speed dependency of **C7H-FS** size.

The diameter of amorphous particles of **C7H-FS** can be controlled from 30 nm to 2.5 μm by the selection of solvents and injection rate of water (Figure 2.8). A condition affording the largest particle (average diameter: 2450 ± 9 nm by statistical analysis of TEM images) was a combination of THF as solvent and slow water injection (0.001 mL/min). The injection rate of water influences the size by changing the degree of supersaturation of **C7H** generated by protonation of **C7K**. The size can be reduced to 168 ± 1 nm by increase of water injection rate to 10 mL/min due to the increase of nucleus number through promoting the supersaturation of **C7H**. Changing solvents from THF to more polar and water-miscible DMF also reduce the average diameter of the particles formed in the suspension, probably because DMF is mixed with water more efficiently than THF, which is known to phase-separate with water at nanoscale,¹⁵ and thus quick supersaturation is achieved to induce more nucleation events.¹⁶ A condition affording the smallest particle (32.5 ± 0.3 nm) was a combination of DMF as a solute and quick water injection (10 mL/min).

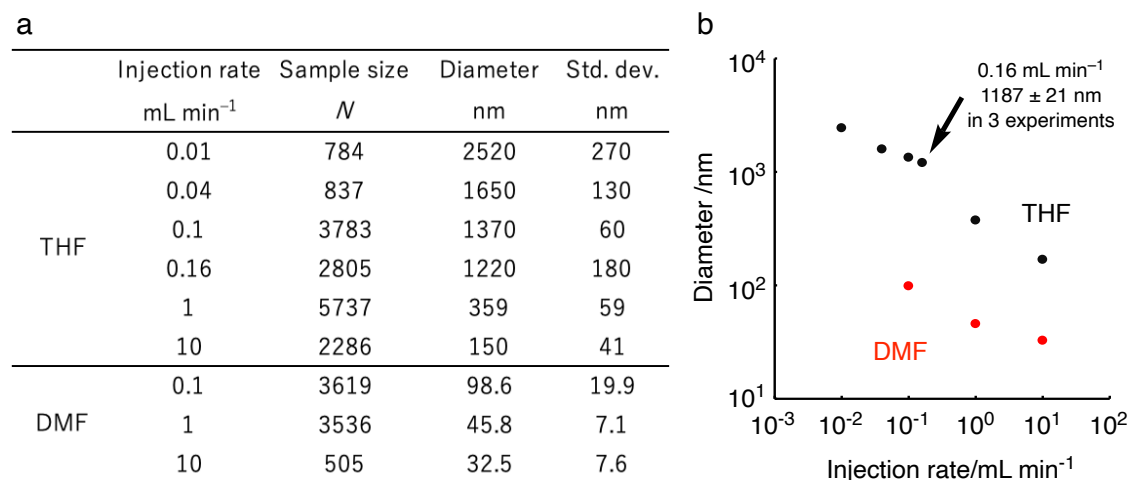


Figure 2.8. Size-control preparation of **C7H**-FS with different water injection rate. (a) A list of experimental parameters and corresponding size information as volume-weighted size distribution. (b) A plot of average diameter of **C7H** -FS against injection rate of water.

2.2.5 Loading of fluorescent dye in **C7H**-FS.

Applicability of **C7H**-FS for the incorporation of water-soluble materials was evaluated by monitoring the incorporation efficiency and spatial distribution of fluorescent dyes in the **C7H**-FS. I prepared rhodamine 6G (R6G)-incorporated **C7H**-FSs by the injection of R6G aqueous solution (1.0 mM) instead of water into **C7K** solution in THF. The excess dye was removed by dialysis and centrifugation to obtain R6G-incorporated **C7H**-FSs. The confocal laser scanning microscopic (CLSM) image of the dried powder showed that incorporation and uniform distribution of R6G into each particle (Figure 2.9b). A line profile of fluorescence intensity on an individual particle is consistent with a uniform distribution of the dye molecule spread over the sphere (Figure 2.9c), suggesting that the amorphous assembly of the **C7H** molecule allows homogeneous mixing with R6G molecules without forming domain structures. By comparing the yield of **C7H**-FS prepared from **C7K** with one prepared from **C7H**, the necessity of the **C7K** as a starting material can be explained clearly (Figure 2.9d). In **C7H** case, the **C7H**-FS yield was much affected by the concentration of solute. With 0.01mM R6Gaq, the yield already decreased to 57.8% but resulted in formations of ill-defined sticky precipitates, while **C7K** systems gave 85.5%. The yield finally decreased to only 1.2 % with 1mM R6G solution, while **C7K** systems still gave 84.1%. The tendency observed in **C7H**-FS formation from **C7H** is a result of salting-out by the existence of ionic solutes in water, and a use of **C7K** is effective for preventing the effect and prepare the **C7H**-FS incorporating guest molecules efficiently.

Chapter 2

Then, I tested the incorporation of other xanthene derivatives with different $\log P$ values (Figure 2.9a). Sulforhodamine B (SRB) is the most hydrophilic dyes ($\log P_{OW} = -2.02$), and Eosin Y (EY) has an intermediate property ($\log P_{OW} = -0.18$). Those dyes-incorporated **C7H**-FSs was purified and dried to the powder forms. Then, they were dissolved to THF/IPA mixed solvent and quantified the molar ratio of dyes against fullerene molecules (Figure 2.9e). I confirmed that even highly hydrophilic dyes (SRB) can be incorporated. By comparing the molar ratios of incorporated dyes, general incorporation tendency was found to correlate well with the $\log P_{OW}$ value (Figure 2.9f), and I assumed that the existence of **C7K** with long lifetimes in water can afford to have hydrophobic interaction with water soluble dyes to load them into **C7H**-FSs.

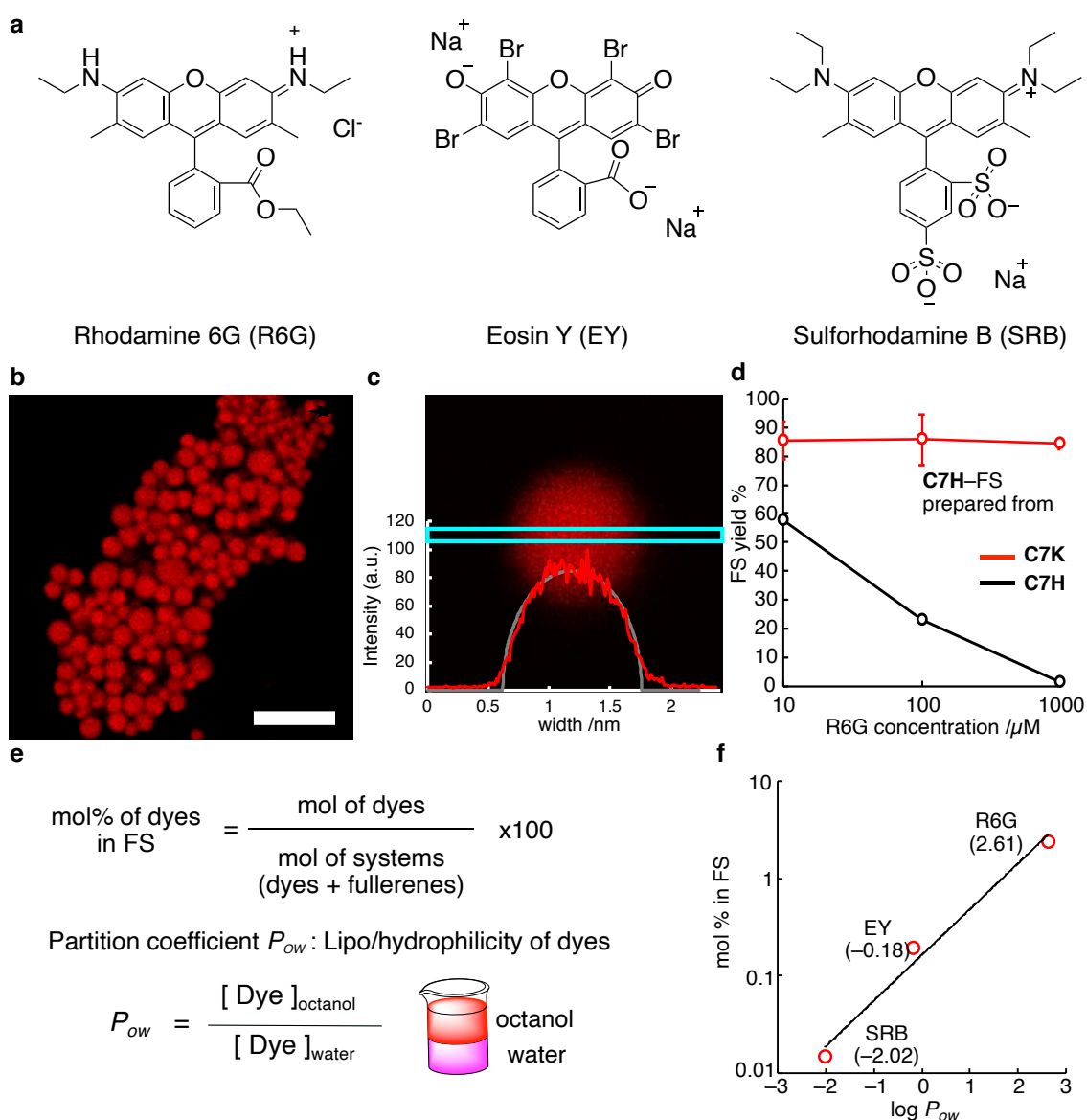


Figure 2.9. Loading of water-soluble xanthene dyes into **C7H**-FS. (a) Molecular structures of xanthene dyes. (b) CLSM image of R6G-containing FS. Scale bar: 5 μm . (c) CLSM image of a single FS with an

Chapter 2

intensity profile for the section of the cyan rectangle. The gray line indicates the calculated fluorescence intensity. (d) The yield of **C7H**-FS prepared by injecting an aqueous R6G solution of various concentrations into a THF solution of **C7K** (red) and **C7H** (black). (f) Amount of dye in **C7H**-FS (mol % dye/**C7H**) plotted against $\log P_{ow}$ (partition coefficients between 1-octanol and water).

2.2.6 Loading of inorganic NPs@FS.

Like the incorporation of R6G from its aqueous solution, water-dispersible nanomaterials like gold nanoparticles (AuNP) and CdSe/ZnS quantum dots (QDs) were found to be incorporated into the **C7H**-FSs. I adjusted the preparation condition to obtain **C7H**-FSs with 30-60 nm sizes for visualizing small nanoparticles with high contrasts in EM images (Figure 2.10c-k). The obtained **C7H**-FSs are isolated by repetitive centrifugation and redispersion with water to remove excess nanoparticles. The embedding ratios of the nanoparticle in the **C7H**-FSs were calculated to be 8-12% by STEM observation when dispersions of the concentration of 5.0×10^{16} particles/L were used (see Figure S2.6 and Table S2.1 in SI).

To visualize NP contrasts in **C7H**-FS with TEM, the property differences between specimen and container must be considered (Figure 2.10 a). Especially, the density of NP is required to be larger than that of FS ($d = 1.25 \text{ g mL}^{-1}$) determined by ultracentrifuge experiments (see Figure S2.5 in SI). As shown in Figure 2.10b, inorganic nanoparticles such as metallic Au, CdSe, and ferrihydrite (utilized by biomolecules in a few example), as well as DNA/RNA, satisfy the requirement, but proteins do not. TEM images of AuNP (5.0 or 15 nm) show its lattice fringe (2.4 Å) assignable to the interplane distance of Au crystals with fcc structure (Figures 2.10c-h). Similarly, TEM images of 6 nm CdSe/ZnS QDs also show lattice fringes (3.7 Å) assignable to the interplane distance of CdSe as core structures of QDs (Figures 2.10i-k). Note that the **C7H**-FS underwent no structural damage induced by electron beam irradiation without any conductive coatings or staining. During the above observations, the structure of **C7H**-FS did not collapse nor deform with total electron dose of $5 \times 10^7 \text{ e}^- \text{ nm}^{-2}$ that supplies enough contrast for atomic-resolution images of lattice structures of the inorganic nanoparticles.

Chapter 2

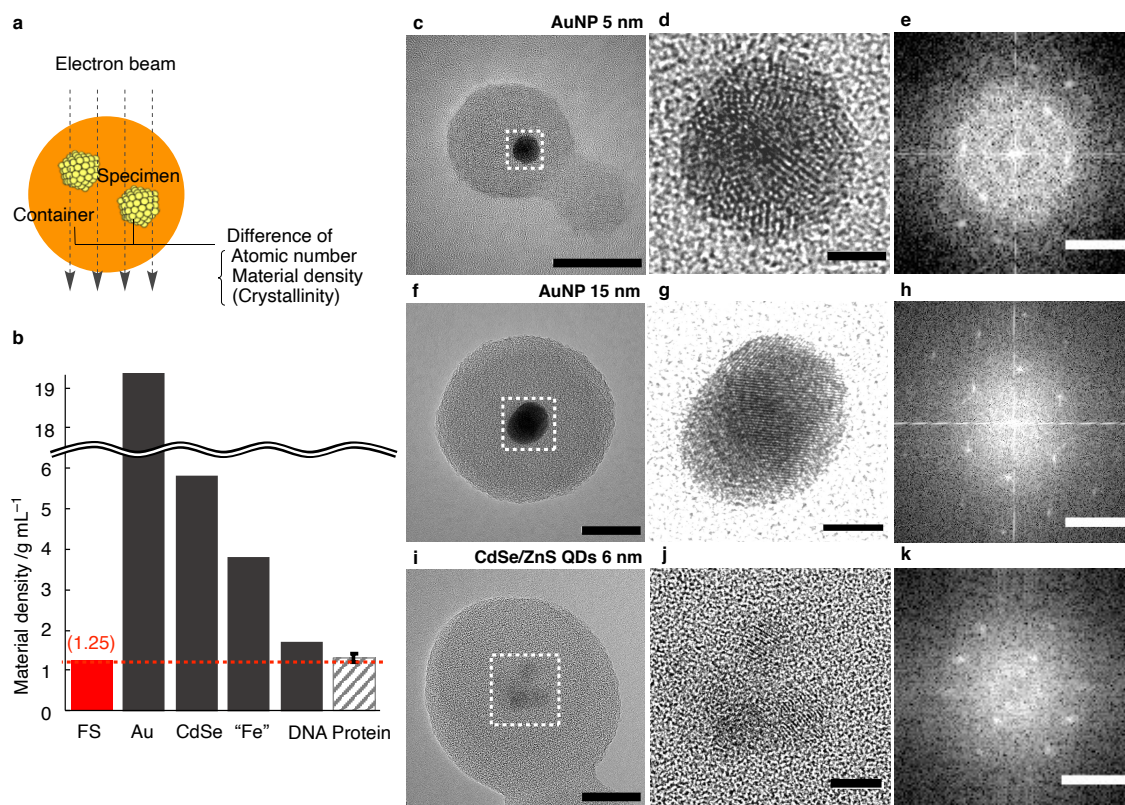


Figure 2.10. TEM images of NPs in C7H-FS. (a) Factors degrading a TEM contrast of specimen in a container. (b) The density of various materials compared with that of C7H-FS. "Fe" denotes ferrihydrite in ferritin. (c-k) TEM image and corresponding fast Fourier transform image of a single AuNP (5 nm, c-e), a single AuNP (15 nm, f-h), and three CdSe/ZnS QDs (6 nm, i-k). Scale bars: 20 nm for c, f, and i, 2 nm for d, 5 nm for g and j, and 5 1/nm for e, h, and k.

2.2.7 Electron tomography of AuNPs@FS.

Electron tomography (ET) is a 3D structural analysis method of nano-size objects¹⁷. The method is composed of following two steps: (a) Image acquisition of the objects from various angles (Figure 2.11a), (b) 3D volume reconstruction by back projection from the collected images (Figure 2.11b)¹⁸. The advantage of ET is an ability to visualize individual specimen structures and a spatial relationship of multiple specimens directly in a real space¹⁹. To analyze the 3D coordinates of specimens, their structures should be enough rigid or fixed by supports like resins or vitreous ice. However, the latter methods often required us the post processing of their fixed structures such as thin sectioning to obtain the specimen contrast. To minimize the process and improve the ET analysis more efficient, I came up the application of **C7H-FS** incorporating nano-size objects based on its property that the size of fullerene shells can be tuned suitable for various target specimens concertedly with their incorporation. The initial ET demonstration was conducted with a **C7H-FS** incorporating 3 AuNPs. The

Chapter 2

AuNPs@**C7H**-FS was prepared in the same protocol described in section 2.2.6, and the prepared sample was directly drop-casted on an amorphous carbon film. The sample was rotated to acquire the series of images in different angles from -60° to $+60^{\circ}$ with 1.0° increments (Figure 2.11c-e). Through the observation, the contrasts of AuNPs in **C7H**-FS were constant even in images at high tilt angles due to spherical shape effect of **C7H**-FS. Then, a volume data of the nanocomposite was reconstructed from the obtained tilt series through the filtered back projection (Figure 2.11f). By utilizing a contrast difference between AuNPs and **C7H**-FSs, the surface structure of each AuNP could be selectively visualized by isosurface rendering and their 3D coordinates probably reflecting their solution states can be determined (Figure 2.11g) which cannot be obtained without a supporting material. Moreover, the system can distinguish the boundary of three AuNPs neighboring less than 1 nm.

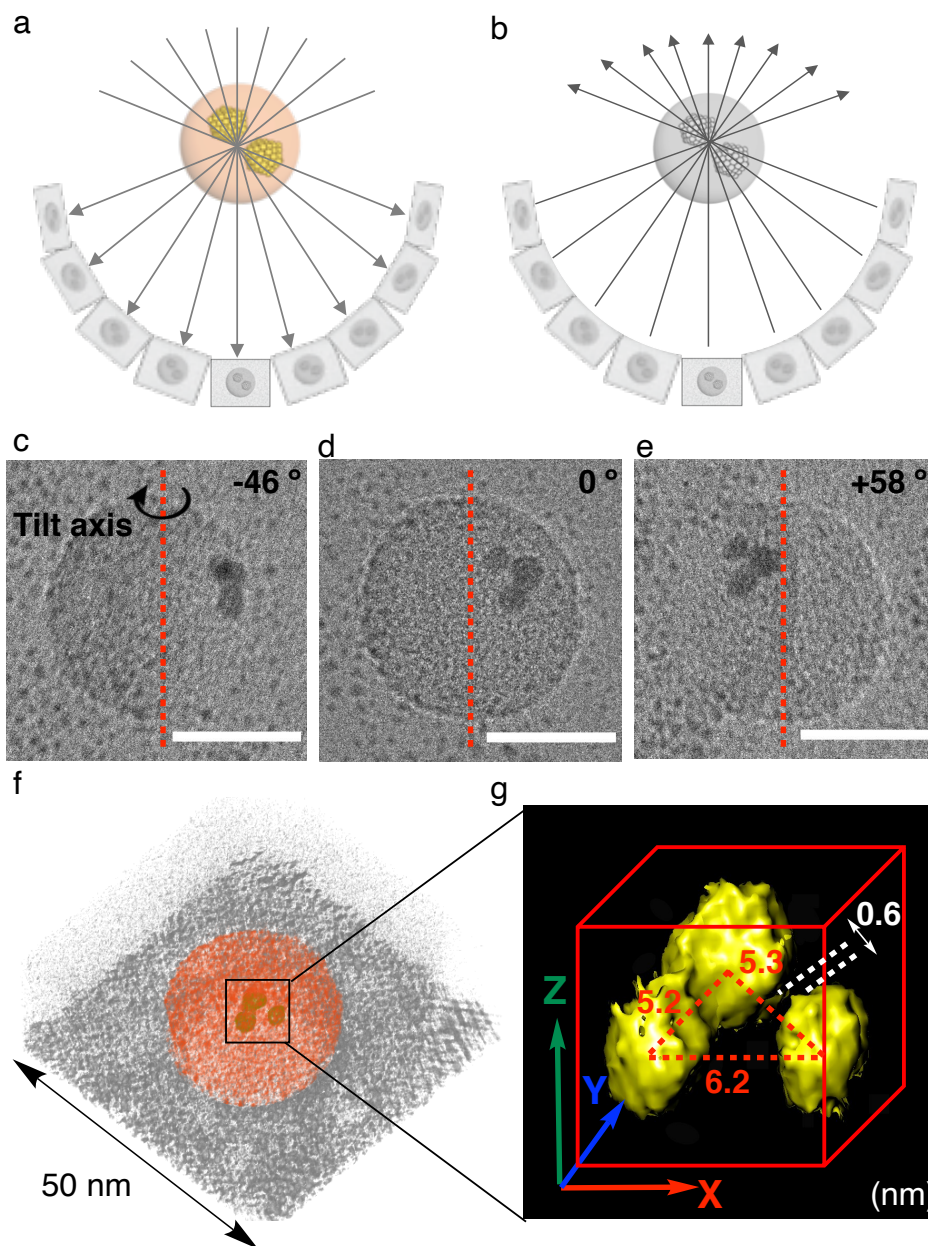


Figure 2.11. Electron tomography analyses on AuNP in C7H-FS. (a) Image acquisition from various angles. (b) 3D volume reconstruction by back projection of the images. (c-e) TEM images of three AuNPs in FS on a 6-nm amorphous carbon film during -46° to $+58^\circ$ tilt on a single axis (red line). Scale bar: 20 nm. (e) A reconstructed AuNPs@FS shown in c-e drawn by a volume rendering. (f) A reconstructed 3D image of AuNPs drawn by an isosurface rendering.

The advantage of C7H-FS as a specimen container is not only its size-controllability but also its spherical structure which retain a constant specimen contrast during rotation. It can solve the problem that the specimen of conventional ET methods is embedded in a plate-like support materials such as sliced resins or vitrified water often

suffering from the difficulty of keeping specimen contrasts²⁰. To maximize the advantage, we applied the **C7H-FS** for ET by suspending individual spheres on the edge of holey carbon grids. Upon deposition of **C7H-FS**s incorporating 5 nm AuNPs dispersed in water to a carbon grid with regular circular holes with 2 μm in diameter (Quantifoil), many spherical particles are found on the side edges of the holes. We chose a sphere which is located on the cross point of the rotating axis and the hole edge, and we collected a series of images with continuous rotation to $\pm 60^\circ$. Figures 2.12b and c show raw images of AuNP@**C7H-FS** during the rotation. It is obvious that the **C7H-FS** can keep its grey contrast during the rotation, while the edge of holey carbon (thickness: 50 nm) became dark. A determination of 3D coordinates of four AuNPs in this experiment (Figure 2.12d) ensure the applicability of **C7H-FS** system for the structural analysis of more complexed structures in the future¹⁹.

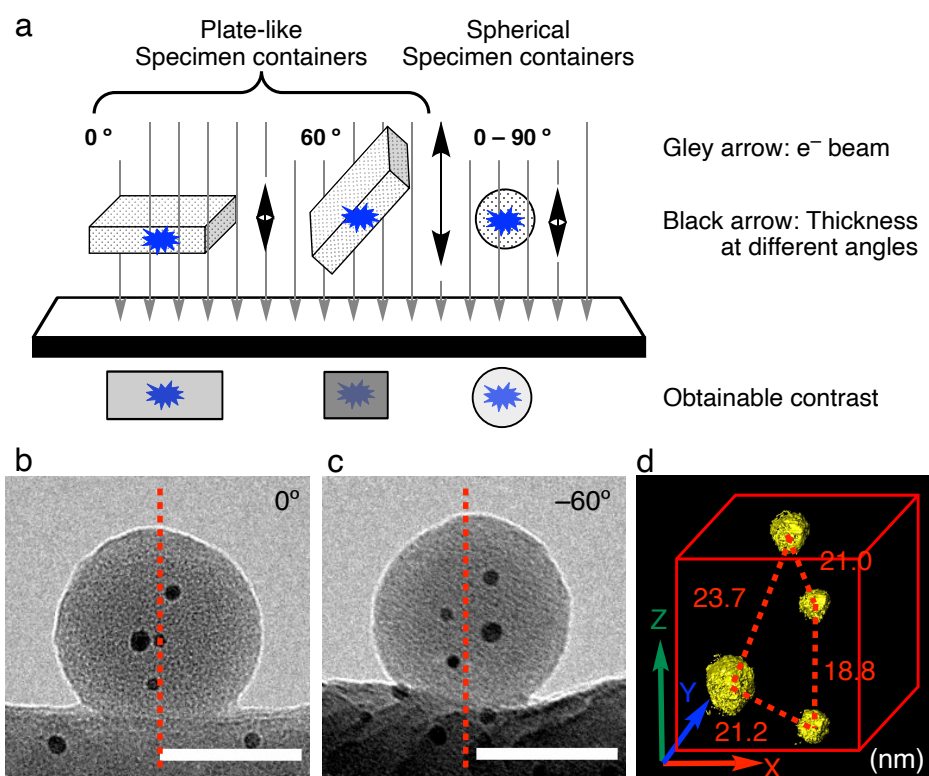


Figure 2.12. A merit of using a **C7H-FS** as a specimen container for electron tomography analyses. (a) A comparison of specimen contrast dependency on the morphology of its container. (b) TEM image of four AuNPs@FS on an edge of a holey carbon film with an in-column omega energy filter. Red lines indicate tilt axis. Scale bar: 50 nm. (c) A -60° tilted TEM image of the specimen in a. (d) Reconstructed image of AuNPs@FS shown in b and c.

2.2.8 Electron tomography of biomaterials@FS.

Proteins and their higher-order assembly can be also incorporated into the **C7H-FS** and are visualized by ET. We slightly modified the preparation condition of **C7H-FS** to incorporate ferritin, proteins incorporating iron(II) clusters, or lambda phage suspended in water (see a section 2.4.12 in SI). Figures 2.13 a and b show a reconstructed structure of a mineral ferrihydrite core of ferritin (Figure 2.13c) giving a clear contrast. The diameter of the observed iron core (6.8 nm) agrees with the reported values (6.8–8.0 nm)²¹, indicating that the **C7H-FS** incorporation preserves the specimen structure. When we prepared the **C7H-FS** with the lambda phage, we trapped a spherical object with 47.6 nm in diameter (Figures 2.13d and e), which is smaller than the inner diameter of capsid (55 nm)^{22,23} and can be attributed to a DNA core. Since the density of **C7H-FS** ($d = 1.25 \text{ g mL}^{-1}$) is similar to that of protein shells, their contrasts of ferritin and lambda phage are buried in the contrast of the surrounding a fullerene shell.

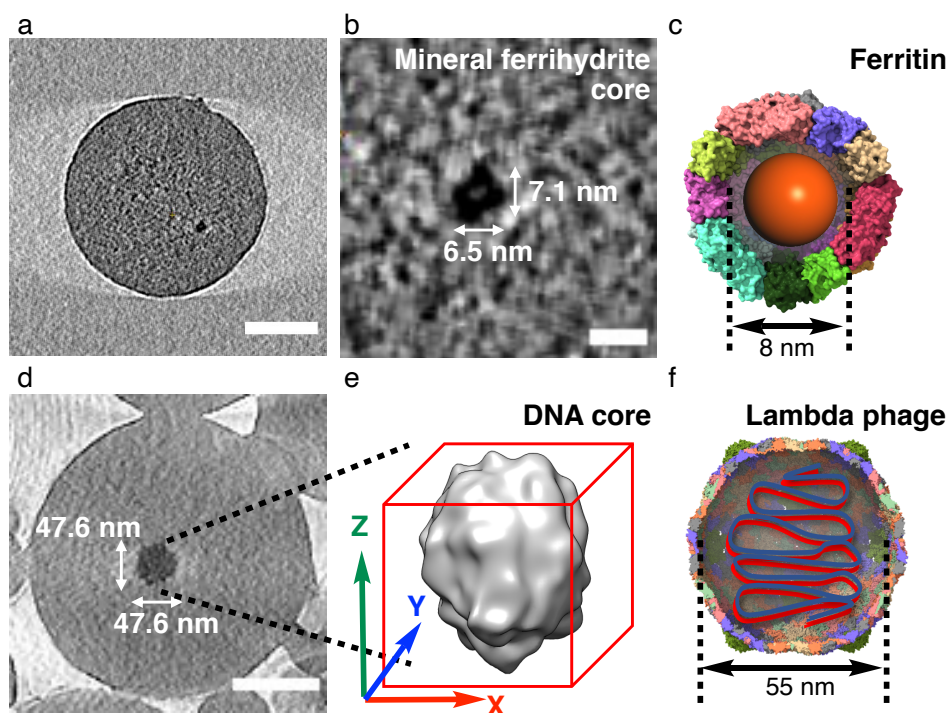


Figure 2.13. Electron tomography analyses on biomaterials in **C7H-FS**. (a) Two-dimensional cross-section view of the 3D reconstructed image of the iron core of ferritin. Scale bar: 50 nm. (b) Magnified image of the core structure in g. Scale bar: 8 nm. (c) Structure of a ferritin containing a ferrihydrite core. (d) Two-dimensional cross-section view of lambda phage in **C7H-FS**. Scale bar: 100 nm. (e) Three-dimensional reconstructed image of the DNA core based on information from four different specimens. (f) Crystal structure of lambda phage and a schematic image of incorporated DNA. The images of the protein shells of i and l were prepared using the UCSF ChimeraX program²⁴ accessing 6PXM and 2FT1 files in the Protein Data Bank Japan.

Chapter 2

2.3 Summary

In the present study, the preparation method of multiple-component nano- and microspheres through molecular assembly of organofullerene was developed. The advantages of the method are its simplicity of preparation process and its applicability for incorporating various nanomaterials inside, compared with the conventional materials based on polymer science. These features were achieved by utilizing the characteristic chemical properties of pentaarylated [60]fullerenes bearing five alkyl groups (**C7H**) that form homogeneously amorphous layer, and its equilibrium between **C7K** and **C7H** in water that control the rate of molecular assembly.

Since the prepared **C7H**-FS has a stable amorphous phase against thermal treatment and electron beam and can fix the 3D coordinates of the incorporated nano-size specimens, the prepared core shell structure was applied for the structural analysis of specimens by ET. Utilizing the advantage of spherical morphology of **C7H**-FS, the incorporated specimen images could be collected with keeping its contrast in a constant at various tilting degrees. **C7H**-FS has a low material density and is applicable not only for structural analysis of inorganic nanoparticles but also biomaterials composed of light elements such as a DNA aggregate of lambda phage in a protein capsid.

Chapter 2

2.4 Experimental section

2.4.1 General

All reactions dealing with air- or moisture-sensitive compounds were carried out in a dry reaction vessel under argon. The water content of the solvent was determined on a Karl–Fischer Moisture Titrator (CA-21, Mitsubishi) to be less than 100 ppm. Flash silica gel column chromatography was performed on silica gel 60N (Kanto, spherical and neutral, 140-325 mesh) as described by Still. High Pressure (Performance) Liquid Chromatography (HPLC) analysis was performed on JASCO HPLC system equipped with Buckyprep column (Nacalai Tesque Cosmosil Buckyprep 4.6 Å~ 250 mm; column temperature at 40 °C). NMR spectra were recorded on a JEOL ECZ-500 (¹H NMR, 500 MHz; ¹³C NMR, 125 MHz) NMR spectrometer. Melting points of solid materials were determined on a Mel-Temp II capillary melting-point apparatus and are uncorrected. Centrifugation was carried out on TOMY MC-150 and LC-100. Dynamic light scattering (DLS) measurement was performed on Malvern Zetasizer Nano ZS equipped with a He-Ne laser operating at 4 mW power and 633 nm wavelength, and a computer-controlled correlator, at a 173° accumulation angle. Measurements were carried out at 25 °C in a polystyrene or glass cuvette. The data were processed using dispersion technology software version 5.10 to obtain Z-average particle size and polydispersity index (Pdl) value by cumulant analysis. Elemental analysis was performed on elemental vario MICRO cube. ICP-AES analysis was performed on Shimadzu ICPS-7510 equipment. UV-Vis absorption spectra in solution (ca. 1.0×10^{-5} M) were measured with a JASCO V-670 spectrometer. Fluorescence spectra was obtained on a JASCO FP-8500 spectrometer. Thermo- gravimetry differential thermal analysis (TG-DTA) was performed on a Rigaku ThermoPlus 2 thermal analyzer (TG 8120). Differential scanning calorimetry (DSC) measurements were performed on NETZSCH DSC204F1. Powder XRD was carried out on a Rigaku Smartlab instrument using Cu K α radiation ($\lambda = 0.1541$ nm) at 25 °C. Scanning electron microscopy (SEM) and scanning transmission electron microscopy (STEM) were performed on FEI Magellan 400L equipped with a retractable STEM detector with BF/DF/HAADF segment.

2.4.2 Materials

Unless otherwise noted, materials were purchased from Tokyo Kasei Co., Aldrich Inc. and other commercial suppliers. Potassium *tert*-butoxide in THF (1.0 M solution) was purchased from Aldrich. Anhydrous ethereal solvents (stabilizer-free) were purchased from KANTO CHEMICAL CO., INC. and purified by a solvent purification system (GlassContour) equipped with columns of activated alumina prior to use. Distilled water was further purified with Millipore Milli-Q. Copper mesh grids precoated with a holey carbon film (NS-C15 for experiments at 298 K and RO-C15 for higher-temperature experiments), with a continuous plastic film (ELS-C10; 20 nm thickness) and with a

Chapter 2

continuous amorphous carbon film (SHR-C075; 6 nm thickness) were purchased from Okenshoji Co. Ltd. Compounds **C0H**, **C1H**, **C7H**, and **C13H** were prepared according to the reported procedure⁸. Tannic acid stabilized gold colloid (diameter 5 nm, 5.47×10^{13} particles/mL in 0.1 mg/ml citrate), amine gold nanoparticles (5000 Da PEG, diameter 5 nm, 2.74×10^{15} particles/mL in USP grade H₂O), carboxylated gold nanoparticles (5000 Da PEG, diameter 5 nm, 2.74×10^{15} particles/mL in USP grade H₂O), citric acid stabilized gold colloid (diameter 15 nm, 1.64×10^{12} particles/mL in 0.1 mg/ml citrate), and CdSe/ZnS alloyed quantum dots (diameter 6 nm, 1 mg/mL in H₂O) were purchased from Cytodiagnostics Inc. Ferritin (from equine spleen Type I approximately 47 mg/mL in saline solution) was purchased from Sigma-Aldrich Co. LLC. Lambda phage (4.2 mg/mL in buffer) was prepared by following the literature.²⁵

2.4.3 Preparation of self-assembled particles of **CnH** by in-situ protonation of **CnK**

Potassium *tert*-butoxide in THF (1.00 M, 24 μ L, 24 μ mol) was added to a suspension (for **C0H** and **C1H**) or solution (for **C7H** and **C13H**) of **CnH** ($n = 0, 1, 7, 13$) (15.7 μ mol) in THF (2.0 mL) and the solution was stirred under nitrogen for 3 h to obtain a dark-orange colored solution of **CnK**. A portion of the solution of **CnK** (7.8 mM, 0.80 mL, 6.2 μ mol) was transferred to a 15 mL Pyrex tube with a magnetic stirring bar replaced with argon, and ultrapure water (4.2 mL, 0.16 mL/min) was injected via a syringe pump (Birmingham gauge of syringe needle: 22G) to the solution while stirring rapidly (500 rpm) at 25 °C. The resulting orange-colored suspension was diluted by ten-fold with ultrapure water and analyzed by DLS.

The **C7H**-FS was also prepared on a larger scale starting from **C7H** (20.0 mg, 12.5 μ mol). The suspensions were diluted by ten-fold with ultrapure water, and the whole suspension was centrifuged at 3,000 g for 5.5 min. After removing the supernatant, the condensed dispersion was diluted with 100 mL of pure water and centrifuged at 3,000 g for 5.5 min. The bottom layer (< 0.05 mL) was collected and redispersed in ultrapure water, suction-filtered through a membrane filter (pore size: 0.1 μ m), and dried in vacuum to obtain 16.1 mg of an orange-colored solid (81% yield) of **C7H**-FS.

2.4.4 SEM/STEM analysis

Samples for SEM/STEM observation of the **CnH** particle were prepared as follows. The suspension of **CnH** was diluted by 100-fold with ultrapure water and centrifuged (Sample volume 1.0 mL in 1.5 mL centrifuge tube, K-factor 4142, 6 mins) to remove salt. The supernatant was removed, and the bottom layer (< 0.05 mL) was mess-up to 1 mL with ultrapure water. A part of the resulting suspension (2 mL) was placed on a TEM grid (ELS-C10) after hydrophilizing for 40 seconds in a TEM grid hydrophilizer (JEOL DII-29020HD) and dried thoroughly under an atmospheric pressure then under vacuum (66 Pa) for 30 min.

Chapter 2

The SEM/STEM observation of the FS was performed on FEI Magellan 400L with a retractable STEM detector at 5×10^{-5} Pa. SEM images were collected by secondary-electron detection mode using a through-lens detector. Beam landing voltage was set to 1 kV, the beam current to 6.3-13 pA, and the working distance to 4 mm. For the STEM observation, beam landing voltage was set to 25 kV, the beam current to 25 pA. The STEM images were collected in a bright field mode.

2.4.5 Density measurement of C7H-FS by ultracentrifugation

To measure the density of C7H-FS, we suspended C7H-FS in aqueous solutions with different density values and tested whether FSs precipitates in each suspension upon ultracentrifugation. Thus, a C7K solution (7.8 mM, 0.8 mL) in DMF was placed to a Pyrex test tube (\varnothing 16 mm) with a magnetic stirring bar, and ultrapure water (4.2 mL) were injected to the solution with a syringe pump (injection rate 0.10 mL/min) with stirring (500 rpm) at 25 °C. The resulting dispersion was centrifuged (Sample volume 1.5 mL in 1.5 mL centrifuge tube, 15,850 g, 45 min), and the supernatant was removed and resuspended in a sucrose aqueous solution with different concentration (density: 1.00–1.30 g mL⁻¹). Ultracentrifugation was carried out on BECKMAN Optima™ TLX with TLA-55 Rotor (186,000 g, 20 min). As C7H-FS kept suspended in 1.25 g/mL sucrose solution (Figure S1), we estimated the density of C7H-FS to be ca. 1.25 g/mL.

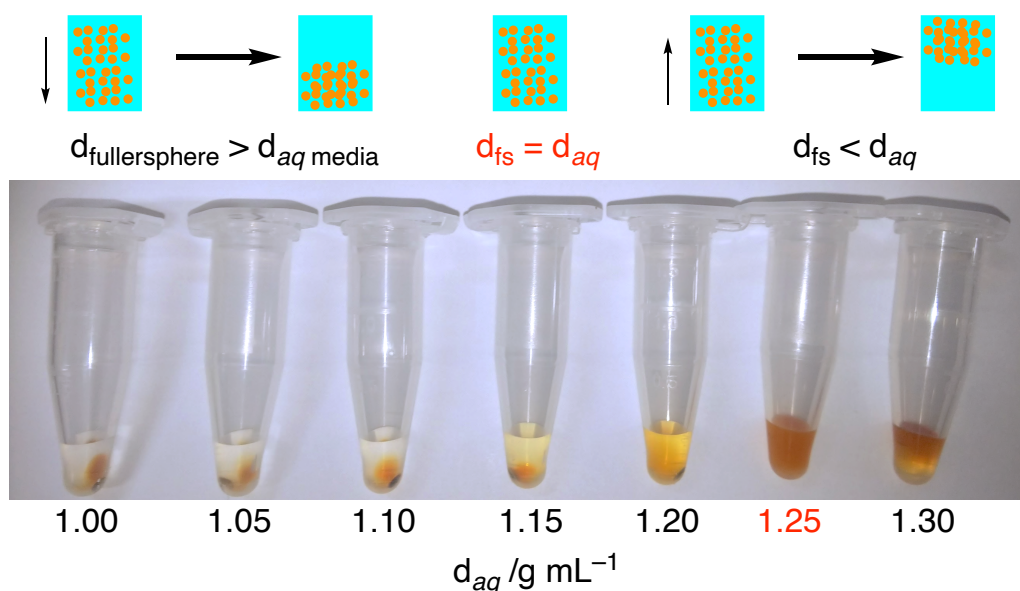


Figure S2.1. Density determination of C7H-FS by ultracentrifugation in sucrose solutions with different density.

Chapter 2

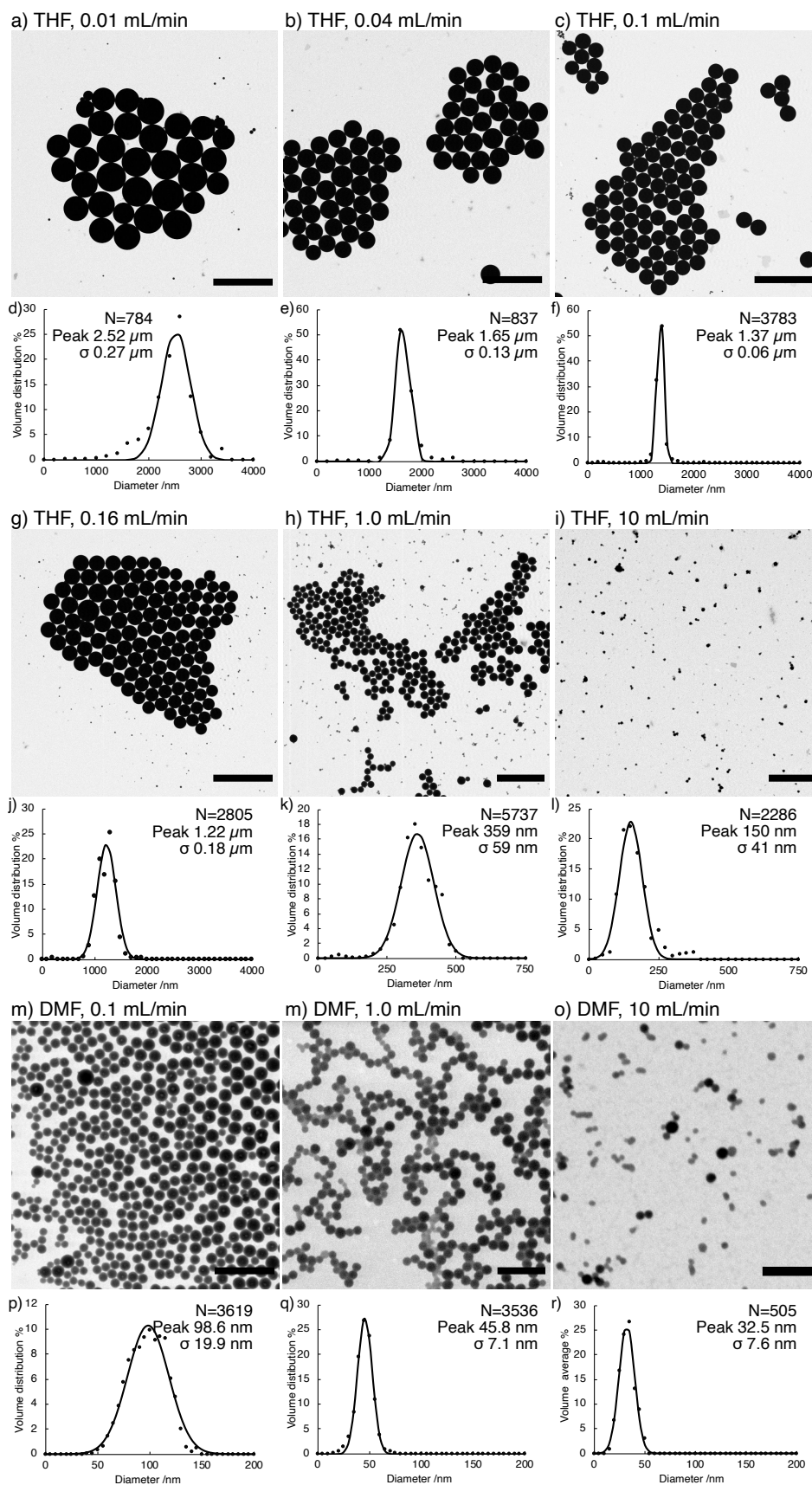
2.4.6 Preparation of C7H-FSs in buffer solution

Glycylglycine-piperazine dichloride buffer (10 mM) was prepared at its pH value of 5.05-9.05 adjusted with NaOH aq. A **C7K** solution (7.8 mM, 0.8 mL, 10.0 mg) in THF was placed in a Pyrex test tube (\varnothing 16 mm) with a magnetic stirring bar, and the prepared buffer (4.2 mL) was injected to the solution with a syringe pump (injection rate 0.16 mL/min) with stirring (500 rpm) at 25 °C. The **C7H**-FS dispersed in supernatant was separated by decantation, and the remaining precipitate of **C7H** was weighed after washing with water followed by drying in vacuum for 66 Pa for 30 min. Yield of the FS was calculated from the weight of the precipitated **C7H**. DLS analysis of **C7H**-FS in the supernatant was carried out in water after replacing the buffered solution with water by centrifugation and dilution.

2.4.7 Preparation of C7H-FSs with different injection rates of water

A **C7K** solution (7.8 mM, 0.8 mL, 10.0 mg) in THF or DMF was placed to a Pyrex test tube (\varnothing 16 mm) with a magnetic stirring bar, and pure water (4.2 mL) was injected to the solution with a syringe pump (injection rate 0.01–10 mL/min) with stirring (500 rpm) at 25 °C. The resulting suspension was centrifuged to remove salt, diluted with water, and transferred to a TEM grid (ELS-C10) for STEM analysis (Figure S1 images). The obtained images were processed by binary and “analyze particle” functions on ImageJ software to collect the individual particle area value, which was converted to volume-weighted diameter distribution as shown in Figure S2.

Chapter 2



Chapter 2

Figure S2.2. Preparation of **C7H**-FSs at different injection rates of water. (a-c, g-i, m-o) Typical STEM images of **C7H**-FSs prepared in conditions described in labels. Scale bars: 5 μm for a-c and g, 2 μm for h-i, 500 nm for n-o. (d-f, j-l, p-r) Volume weighted size distribution corresponding to a-c, g-i and m-o, respectively.

2.4.7 TG-DTA of **C7H**-FS

TG analysis was performed on Rigaku Thermo Plus TG 8210. Powder of **C7H**-FS (ca. 4 mg) was heated to 600°C in alumina crucibles at a rate of 7 K/min, then kept at 600 °C for 60 min. The measurement was carried out under nitrogen flow at a flow rate of 200 mL/min.

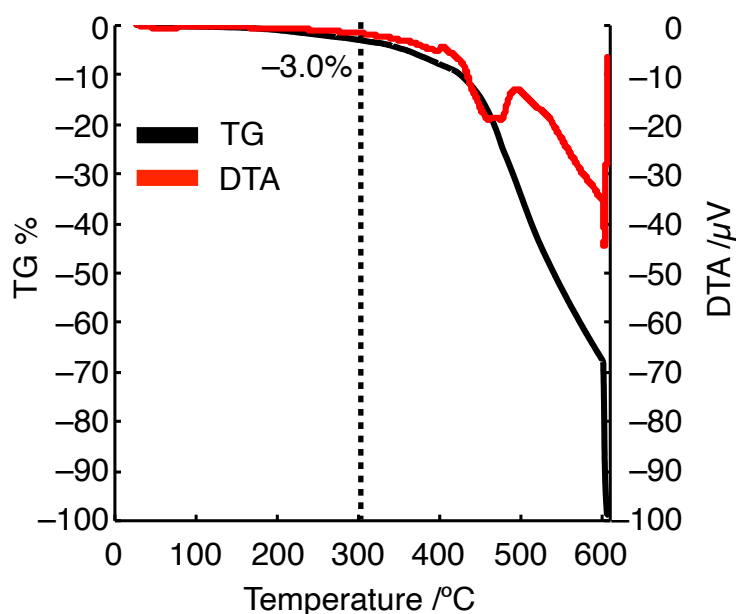


Figure S2.3. TG-DTA chart of bulk **C7H**-FS showing its thermal stability up to 300 °C.

2.4.8 DSC analysis

DSC measurement was performed on NETZSCH DSC204F1. In a typical experiment, the sample (3–5 mg) was sealed in a 25 μL aluminum pan with ~ 0.1 mm hole in the lid. A blank pan was used as a reference. At the start of each experiment, the sample was equilibrated at 20 °C for 15 min. All the experiments were conducted under nitrogen flow at a flow rate of 20 mL/min. For low temperature experiments, liquid nitrogen was used as a coolant.

Chapter 2

2.4.8 TEM and selected-area electron diffraction (SAED) analysis of C7H-FS at 25–300 °C

TEM observation was carried out on a JEM-ARM200F transmission electron microscope (JEOL, Ltd.) equipped with an aberration corrector and cold-field emission gun (point resolution: 0.10 nm) operated at 80 kV and 200 kV, under 1×10^{-5} Pa in the specimen column and with typical Cs values of 1–3 μm . A specimen-loaded grid was operated with a double-tilt holder EM-01030RSTH (JEOL, Ltd.) at 25 °C or a heating holder EM-21130 (JEOL, Ltd.) above 25°C. TEM images and SAED patterns were taken with OneView camera (Gatan, Inc.). The data were collected as a .dm3 format file on DigitalMicrograph software (Gatan, Inc.) and processed using ImageJ 2.1.0/1.53c software.²⁶ The average diameter change upon heating of C7H-FSs to 300 °C was $-1.3\% \pm 0.7\%$ for five particles.

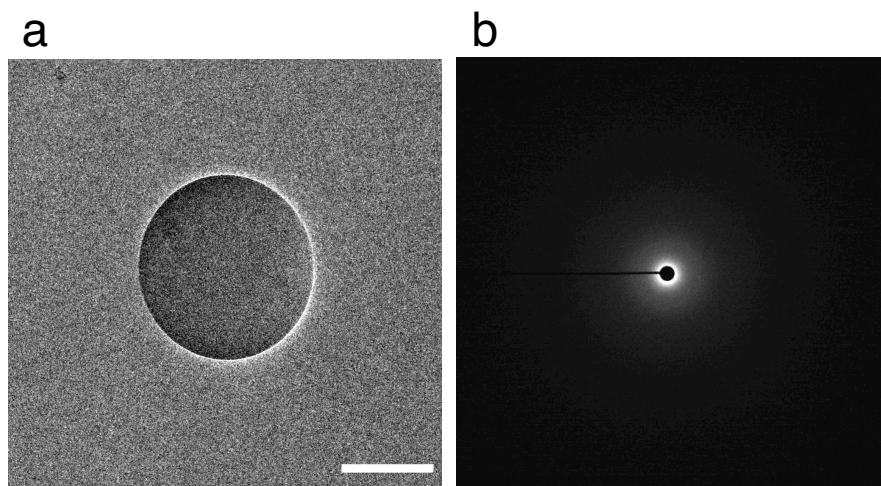


Figure S2.4. TEM observation of C7H-FS. (a) TEM image of a C7H-FS at 25 °C. Scale bar: 500 nm. (b) SAED image of the C7H-FS showing no diffraction spots.

2.4.9 TEM and SAED analysis of C7H-FS at –181 °C

The TEM observations were carried out on a JEM-2010F transmission electron microscope (JEOL, Ltd.) operated at 200 kV. A specimen-loaded grid was operated with a 626 cryo-transfer holder (Gatan, Inc.). For observation at –181 °C, the holder with the specimen was inserted into the microscope and gradually cooled to –181 °C over 60 min before observation. Images of the specimens were acquired with a TemCam-F416 camera and an EM-Menu control software (TVIPS, GmbH). SAED patterns were recorded on SO-163 film developed in D19 (Eastman Kodak Company) at 20°C for 14 min and scanned using a Super COOLSCAN 9000 ED film scanner (Nikon, Co.). The average diameter change upon cooling of C7H-FSs to –181 °C was $-0.4\% \pm 0.7\%$ for six particles.

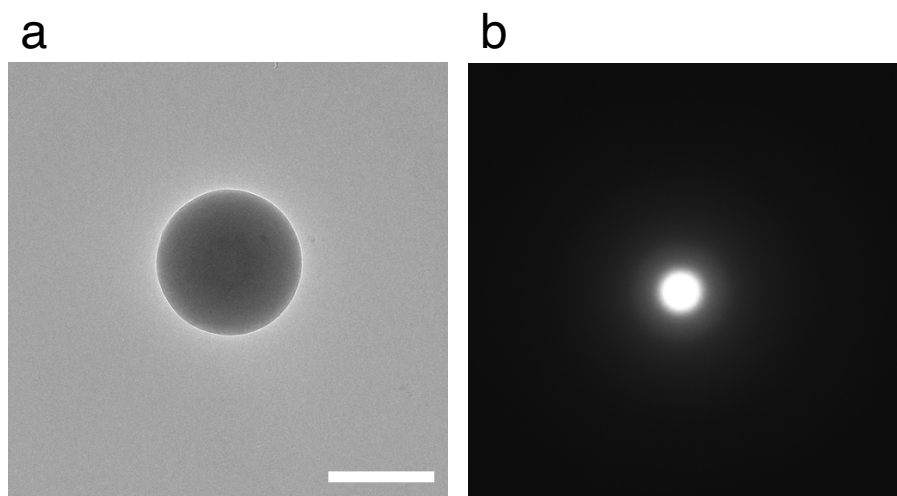


Figure S2.5. TEM observation of **C7H-FS** at $-181\text{ }^{\circ}\text{C}$. (a) TEM image of a **C7H-FS** at $-181\text{ }^{\circ}\text{C}$. Scale bar: 500 nm. (b) SAED image of the **C7H-FS** showing no diffraction spots.

2.4.10 Preparation of **C7H-FS** incorporating fluorescent dyes

For the preparation of **C7H-FS** incorporating rhodamine 6G (R6G), a **C7K** solution (7.8 mM, 0.8 mL, 10.0 mg) in THF was placed to a Pyrex tube (\varnothing 16 mm) with a magnetic stirring bar, and R6G solution (0.010, 0.10, 1.0 mM, 4.2 mL) in water was injected to the solution with a syringe pump (injection rate: 0.16 mL/min) with stirring (500 rpm) at $25\text{ }^{\circ}\text{C}$, which resulted in a pink suspension containing R6G@**C7H-FS**. The **C7H-FS** dispersed in supernatant was separated by decantation, and the remaining precipitate of **C7H** was weighed after washing with water followed by drying in vacuum for 66 Pa for 30 min.

For confocal laser scanning microscopic (CLSM) observation, R6G@**C7H-FS** prepared from R6G solution (1.0 mM) was subjected to centrifugation for 20 min (3,000 g), and the supernatant was removed and resuspended in ultrapure water. The centrifugation process was repeated until the supernatant became colorless (no unbound R6G remaining). The resulting suspension was filtrated and dried in a vacuum desiccator (66 Pa) for 8 h to obtain red powder of R6G@**C7H-FS** (5.0 mg), which was subjected to CLSM observation.

C7H-FS containing eosin Y or sulforhodamine B was prepared by injecting 1.0 mM dyes solution in water in the same procedure as that of R6G. The dye-loaded FS was isolated as powder through dialysis and centrifugation followed by freeze-drying at 20 Pa. The isolated dye-incorporating FS was dissolved in THF/2-propanol (1/1, ca. $1.0 \times 10^{-6}\text{ M}$), which was subjected to fluorescent spectrum measurement to obtain the mol% of dye molecules in the FS (Figure 6d).

Chapter 2

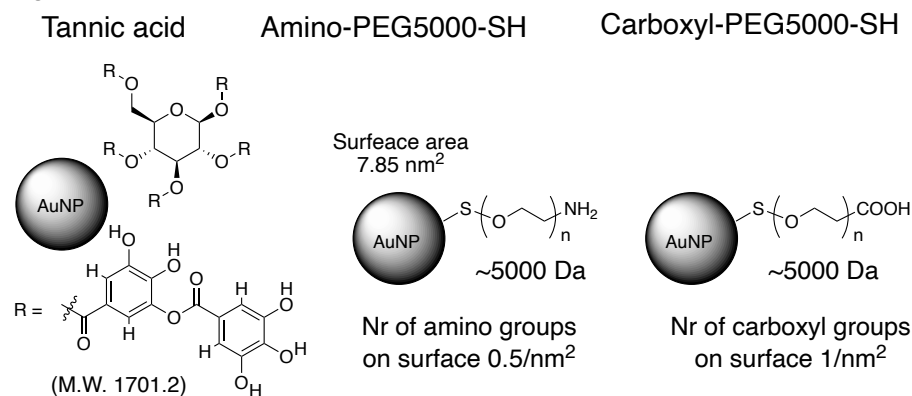
2.4.11 CLSM analysis of R6G@C7H-FS

CLSM analysis was performed on an Olympus Fluoview FV 3000 confocal microscope, controlled by FV31S-SW software. The powder of R6G@C7H-FS was deposited on a clean microscope cover slide and covered by 17 μm thick coverslip. R6G in C7H-FS were excited at 561 nm using a mercury lamp. The images were collected using an oil immersion objective (oil refractive index 1.55).

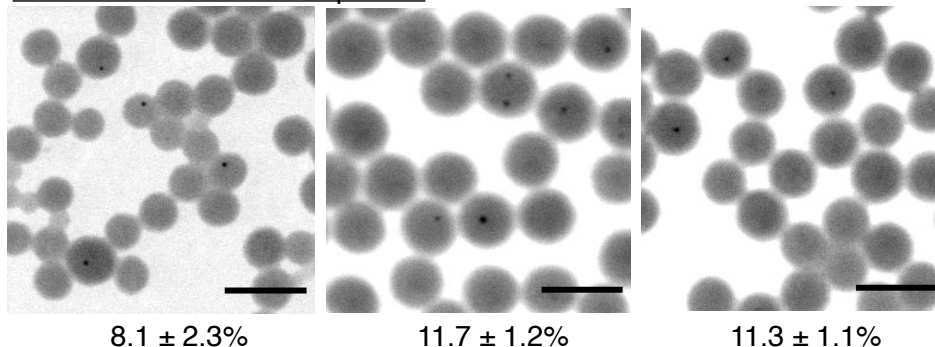
2.4.12 Incorporation of nanomaterials into C7H-FSs

For incorporation of inorganic nanoparticles such as AuNPs and CdSe/ZnS quantum dots, a C7K solution (7.8 mM, 0.2 mL) in DMF was placed to a Pyrex test tube (\varnothing 10 mm) with a magnetic stirring bar, and 50 μL of nanoparticle solution in aqueous media followed by ultrapure water (2.0 mL) was injected to the solution with a syringe pump (injection rate 2.5 mL/min) with stirring (1000 rpm) at 25 $^{\circ}\text{C}$. The resulting dispersion was further diluted by 50-fold with ultrapure water and centrifuged (Sample volume 1.0 mL in 1.5 mL centrifuge tube, K-factor 460, 70 min) to remove salts. The supernatant was removed by decantation, and the remaining suspension (< 0.05 mL) were diluted with ultrapure water to obtain 1 mL dispersion of nanoparticle-loaded C7H-FS.

Ligand



Ratio of Au-loaded fullerspheres



Chapter 2

Figure S2.6. Incorporation efficiency of 5 nm AuNPs from their dispersions (5.5×10^{16} particles L^{-1} in water/buffer). Scale bar: 100 nm.

Table S2.1. Incorporation efficiency of 5 nm AuNPs from their dispersions (5.5×10^{16} particles L^{-1} in water/buffer)

Ligand	Conc. (Num./L)	[fullerspheres incorporating specimens] / [total fullerspheres] (%)				
		Ent1	Ent2	Ent3	Average	Std. error
tannic acid	5.50×10^{16}	4.0	11.8	8.6	8.1	2.3
HS-PEG-NH ₂	5.46×10^{16}	12.8	9.4	13.0	11.7	1.2
HS-PEG-CO ₂ H	5.46×10^{16}	12.0	9.1	12.9	11.3	1.1

For incorporation of biological materials such as ferritin and lambda phage, a **C7K** solution (7.8 mM, 0.8 mL) in DMF were placed to a Pyrex test tube (\varnothing 16 mm) with a magnetic stirring bar, and the targeted specimens in aqueous media (4.2 mL) were injected to the solution with a syringe pump (injection rate 0.10 mL/min) with stirring (500 rpm) at 40 °C. The resulting suspensions were subjected to centrifugation for 20 min (4,500 g), the supernatant was removed and resuspended in ultrapure water. The purification processes were repeated by two times.

2.4.13 Electron tomography (ET) of C7H-FS incorporating AuNPs on the edge of a holey carbon film

The particles of **C7H-FS** incorporating 5 nm AuNPs in milliQ were adsorbed on holey carbon coated copper grids (Quantifoil Micro Tools, GmbH) with fiducial markers (5 nm AuNPs). The grids were transferred into Talos-Artica (Thermo Fisher Scientific, Inc.). Single-axis tilt series were recorded at -181 °C using a K2 Bioquantum camera (Gatan, Inc.) and SerialEM software for automated image acquisition (PMID: 16182563). The angular range of the tilt series was from -50° to 60° with 2.0° increment. Total electron dose was limited to approximately 1.0×10^5 $e^- \text{ nm}^{-2}$. Images were recorded at 200 kV, with -1.5 μm defocus, at a pixel size of 0.103 nm. An in-column omega energy filter was used to enhance the image contrast in the zero-loss mode with a slit width of 25 eV. The tilt series images were aligned and back projected to reconstruct 3D tomograms using TEMography software (System In Frontier, Inc.).

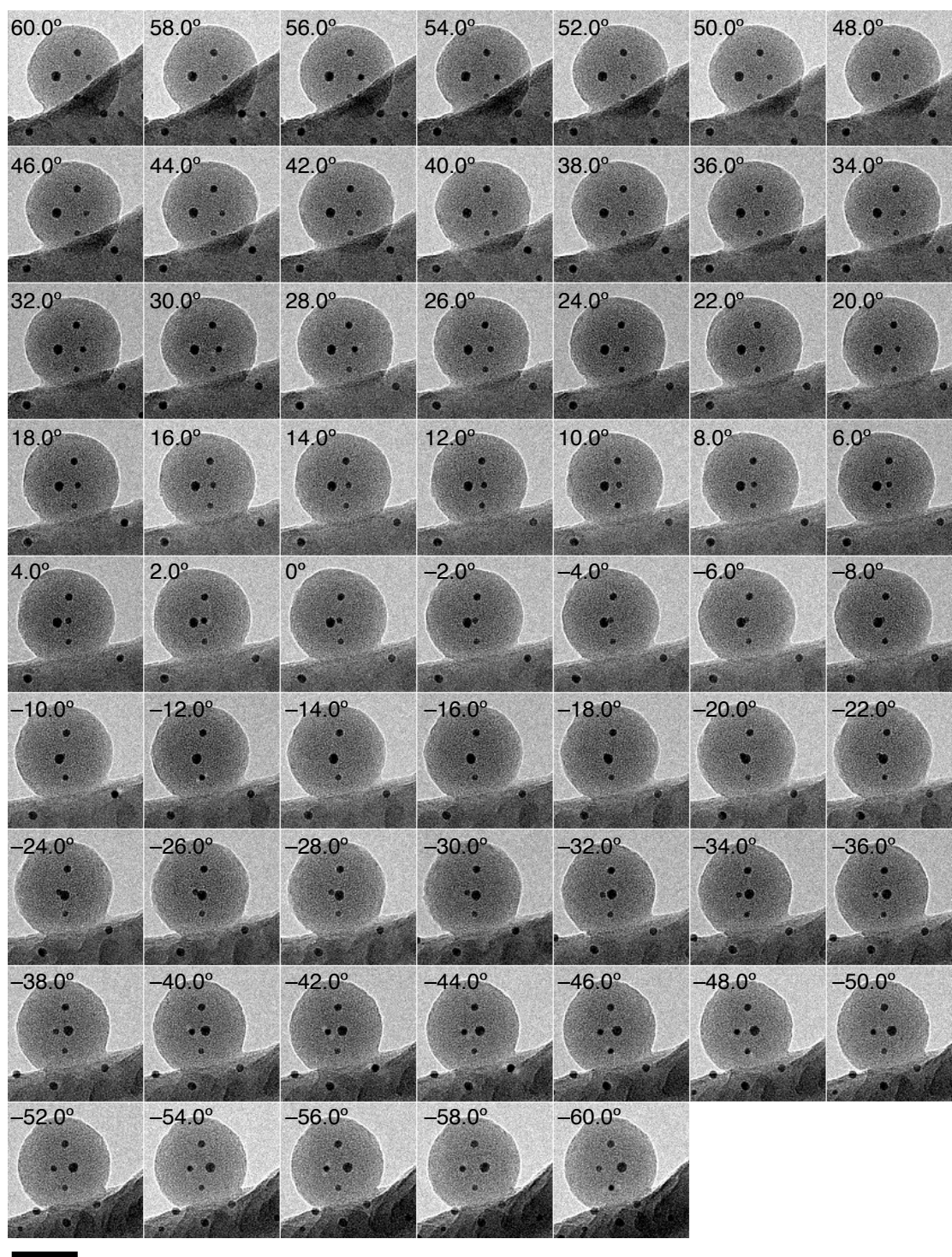


Figure S2.7. Tilt series of 61 projections acquired from AuNP@FS on the edge of a holey carbon film with a single tilt axis. Scale bar: 50 nm.

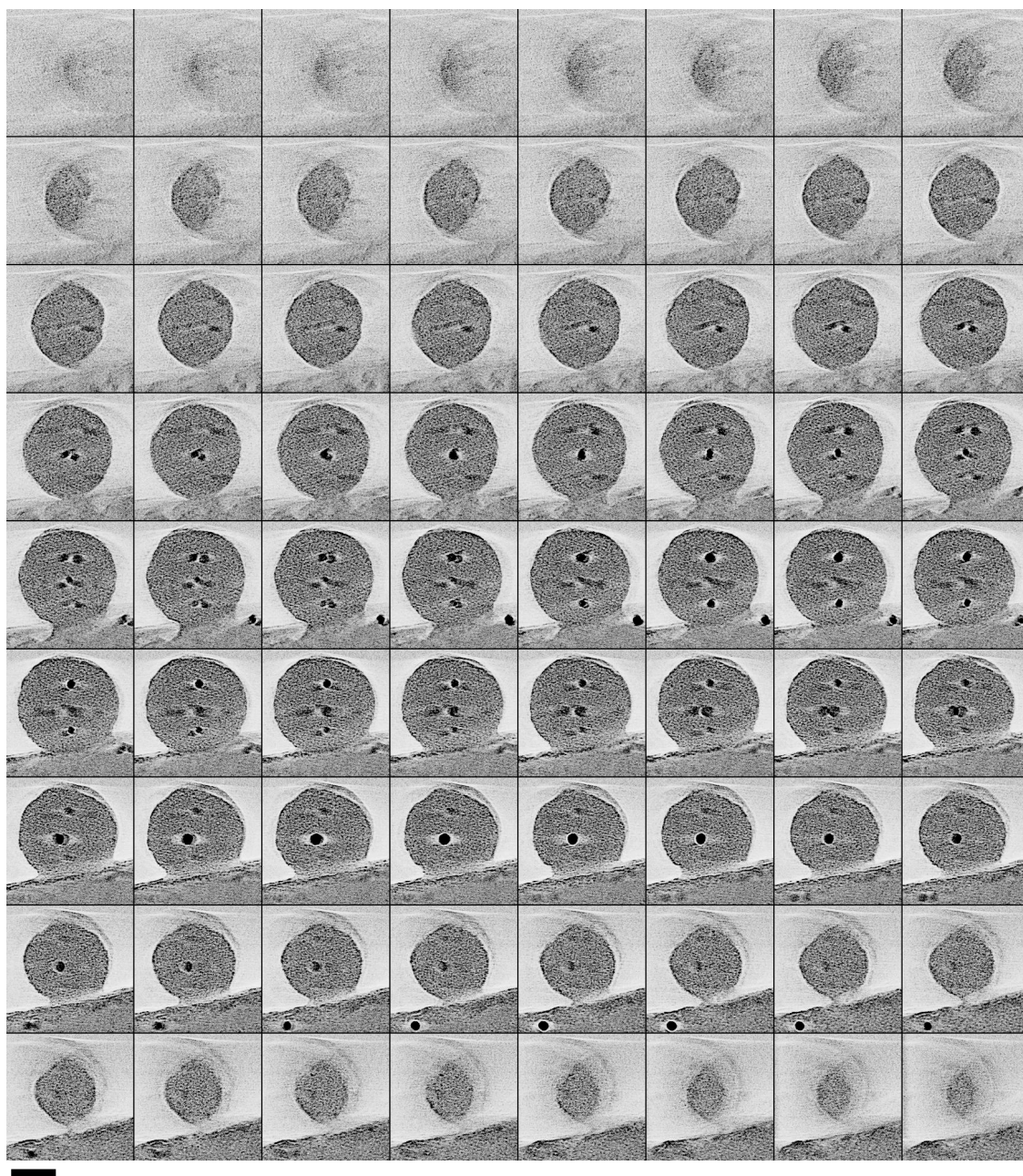


Figure S2.8. Multi slices in the X-Y plane (slice interval in above montage image: 1.03 nm along with Z-axis) obtained from the reconstructed AuNP@FS on the edge of a holey carbon film. Scale bar: 30 nm.

2.4.14 ET of C7H-FS incorporating AuNPs on continuous carbon film

C7H-FSs incorporating 5 nm AuNPs in milliQ were adsorbed on a TEM grid (SHR-C075, film thickness: 6 nm) with fiducial markers (1.5 nm AuNPs). The grids were transferred into a JEM-ARM200F transmission electron microscope (JEOL, Ltd.). Single-axis tilt series were recorded at 25 °C using a K2-IS camera (Gatan, Inc.) operated

Chapter 2

in summit mode and TEMography software for automated image acquisition. The angular range of the tilt series was from -50° to 60° with 1.0° increment. Total electron dose was limited to approximately $2 \times 10^5 \text{ e}^- \text{ nm}^{-2}$. Images were recorded at 200 kV, with -200 nm defocus, at a pixel size of 0.052 nm . The tilt series images were aligned and back projected to reconstruct 3D tomograms using TEMography.

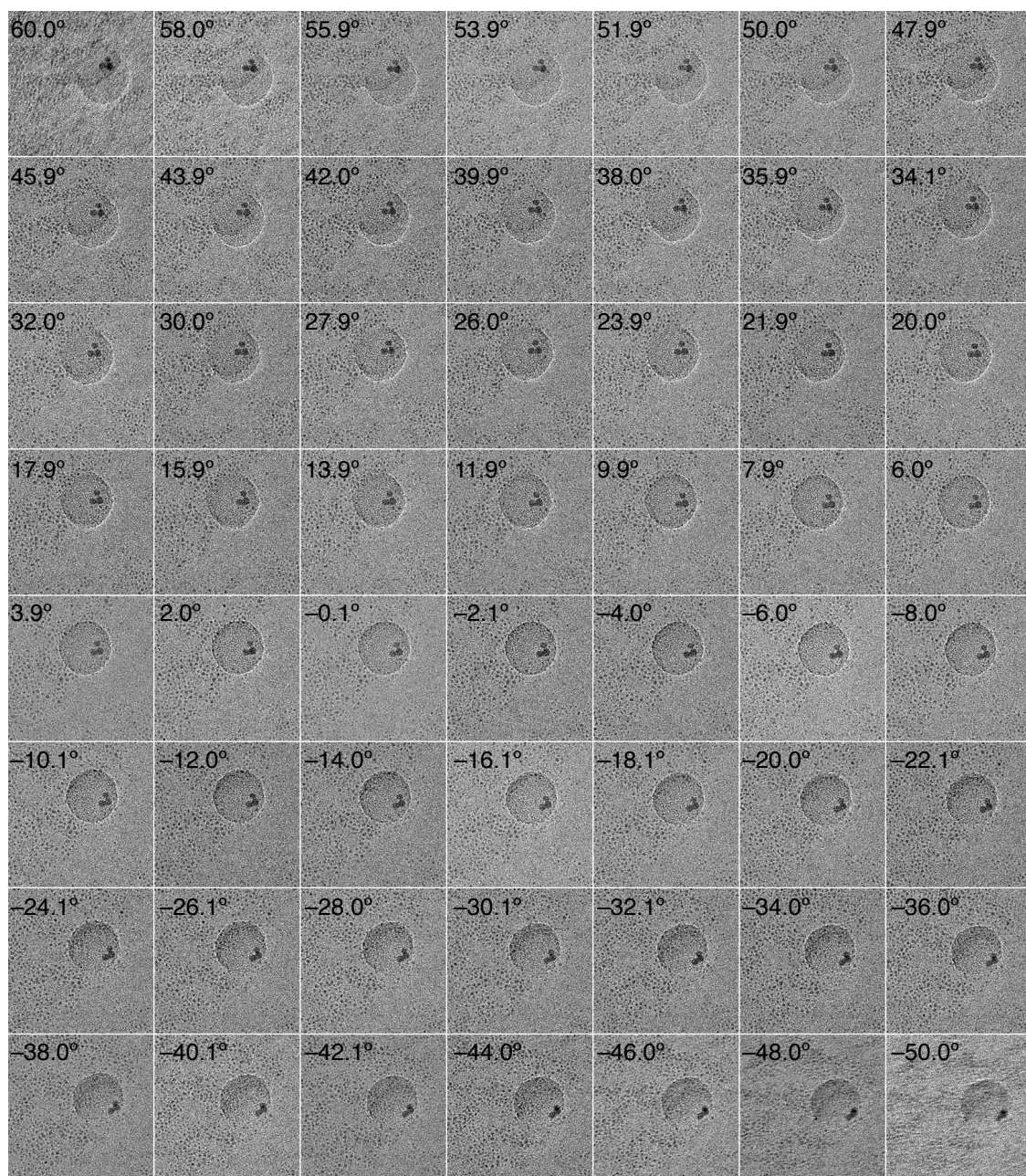


Figure S2.9. Tilt series of 111 projections acquired from AuNP@FS on a continuous carbon film with a single tilt axis. Scale bar: 30 nm .

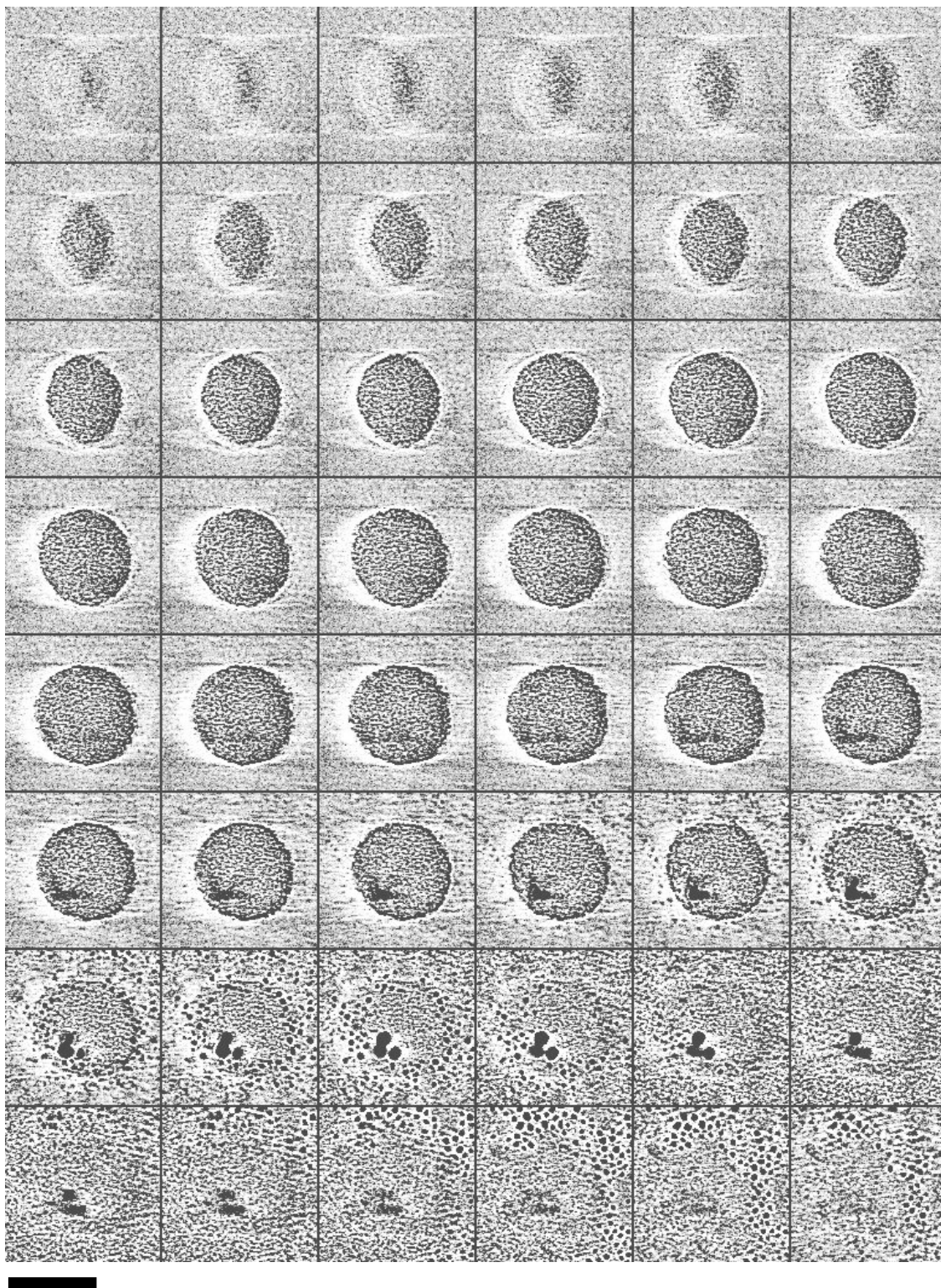


Figure S2.10. Multi slices in the X-Y plane (slice interval in above montage image: 0.83 nm along with Z-axis) obtained from the reconstructed AuNP@FS on a continuous carbon film. Scale bar: 30 nm.

Chapter 2

2.4.15 ET of C7H-FS incorporating biomolecules on continuous carbon film

C7H-FSs were adsorbed on carbon coated copper grids with BSA-coated 15-nm gold colloid particles (#215.133, Aurion) for fiducial markers. The grids were transferred into a JEM-3100FEF transmission electron microscope (JEOL, Ltd.) with an EM-21311HTR high-tilt holder (JEOL Ltd.). Single-axis tilt series were recorded at 20 °C using a K2 summit camera (Gatan, Inc.) and SerialEM software. The angular range of the tilt series was from -60° to 60° with 2.0° increments. Total electron dose was limited to approximately $1.5 \times 10^4 \text{ e}^{-} \text{ nm}^{-2}$. Images were recorded at 300 kV, with $-6.0 \mu\text{m}$ defocus, at a pixel size of 0.43 nm for ferritin-incorporated FS and 0.71 nm for lambda-phage incorporated FS. An in-column omega energy filter was used to enhance the image contrast in the zero-loss mode with a slit width of 25 eV. The tilt series images were aligned and back projected to reconstruct 3D tomograms using IMOD software (PMID: 8742726).

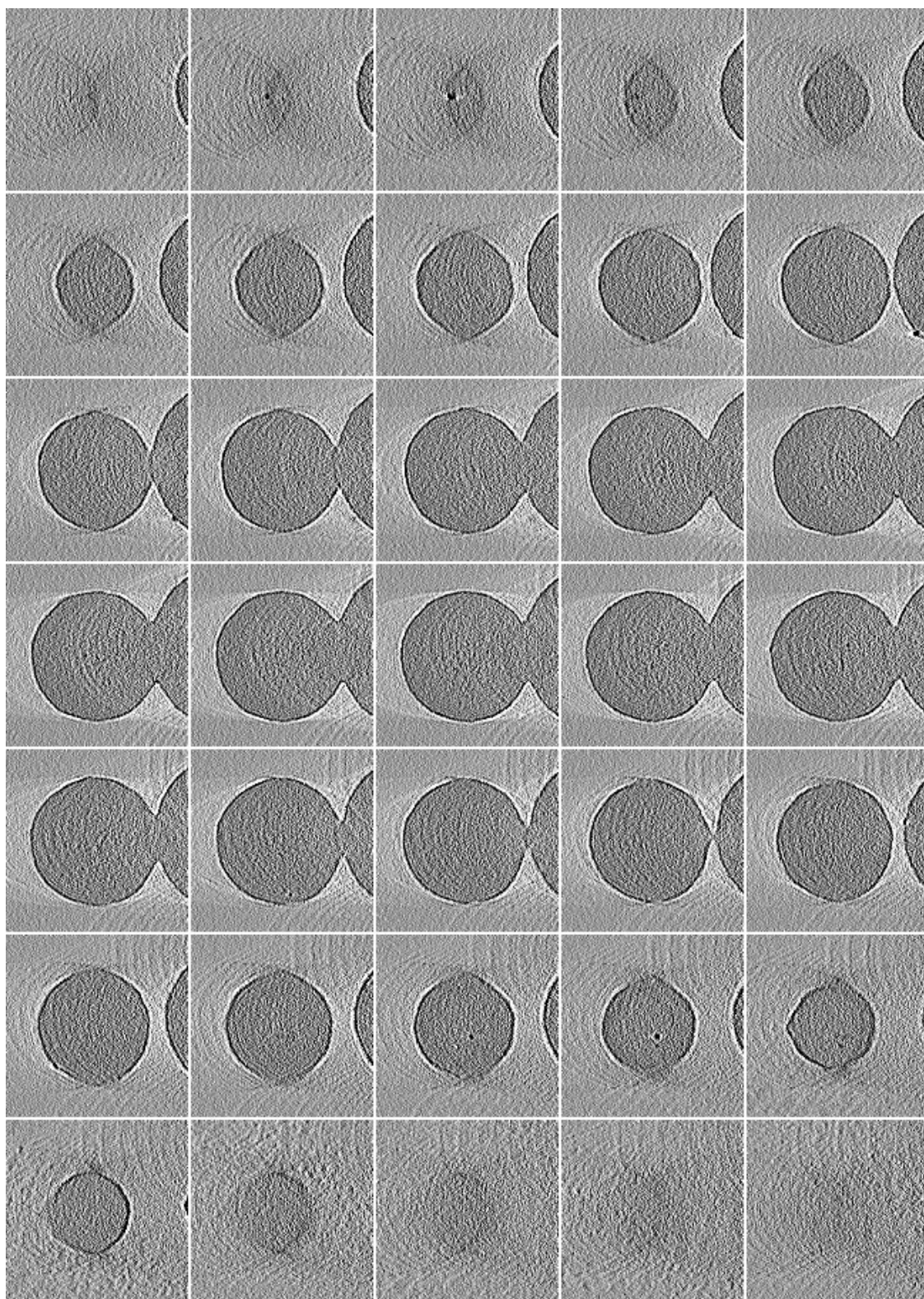


Figure S2.11. Multi slices in the X-Y plane obtained from the reconstructed ferritin@FS on a continuous carbon film. Scale bar: 50 nm.

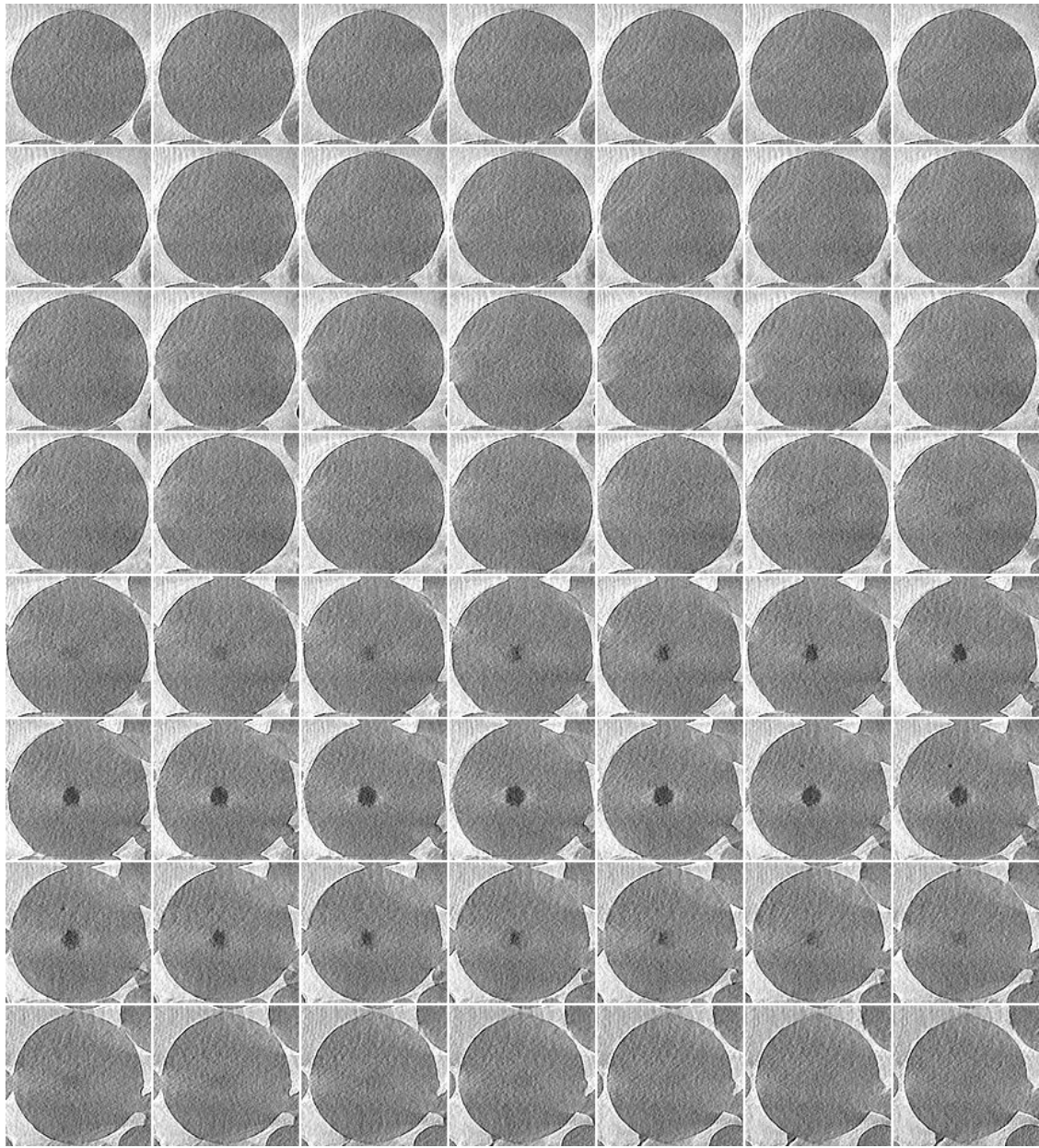


Figure S2.12. Multi slices in the X-Y plane obtained from the reconstructed lambda phage@FS on a continuous carbon film. Scale bar: 100 nm.

Chapter 2

2.5 References

- 1) Chaundhuri, R. G.; Paria, S. Core/Shell Nanoparticles: Classes, Properties, Synthesis Mechanisms, Characterization, and Applications. *Chem. Rev.* **2012**, *112*, 2373–2433.
- 2) Ramli, R. A.; Laftah, W. A.; Hashim, S. Core-shell polymers: a review. *RSC Adv.* **2013**, *3*, 15543–15565.
- 3) Yang, P.; Murase, N.; Suzuki, M.; Hosokawa, C.; Kawasaki, K.; Kato, T.; Taguchi, T. Bright, non-blinking, and less-cytotoxic SiO₂ beads with multiple CdSe/ZnS nanocrystals. *Chem. Commun.* **2010**, *46*, 4595–4597.
- 4) Chen, Z.; Cui, Z.; Niu, F.; Jiang, L.; Song, W. Pdnanoparticles in silica hollow spheres with mesoporous walls: a nanoreactor with extremely high activity. *Chem. Commun.* **2010**, *46*, 6524–6526.
- 5) Kochuveedu, S.; Son, T.; Lee, Y.; Lee, M.; Kim, D.; Kim, D. H. Revolutionizing the FRET-Based Light Emission in Core-Shell Nanostructures via Comprehensive Activity of Surface Plasmons. *Sci Rep* **2014**, *4*, 4735.
- 6) Pan, M.; Sun, Y.; Zheng, J. Boronic Acid-Functionalized Core-Shell-Shell Magnetic Composite Microspheres for the Selective Enrichment of Glycoprotein *ACS Appl. Mater. Interfaces.* **2013**, *5*, 8351-8358.
- 7) Morikawa, M.; Murata, K.; Yamada, K.; Kimizuka, N. Controlled Formation of Microspheres from Ferrocene-derivatized Amino Acids in Binary Aqueous/Organic Media. *Chem. Lett.* **2013**, *42*, 501–503.
- 8) Homma, T.; Harano, K.; Isobe, H.; Nakamura, E. Preparation and Properties of Vesicles Made of Nonpolar/Polar/Nonpolar Fullerene Amphiphiles. *J. Am. Chem. Soc.* **2011**, *133*, 6364-6370.
- 9) Hamasaki, R.; Matsuo, Y.; Nakamura, E. Synthesis of Functionalized Fullerene by Mono-alkylation of Fullerene Cyclopentadienide. *Chem. Lett.* **2004**, *33*, 328.
- 10) Homma, T.; Harano, K.; Isobe, H.; Nakamura, E. Nanometer-Sized Fluorous Fullerene Vesicles in Water and on Solid Surfaces. *Angew. Chem. Int. Ed.* **2010**, *49*, 1665-1668.
- 11) Bairi, P.; Minami, K.; Hill, J. P.; Nakanishi, W.; Shrestha, L. K.; Liu, C.; Harano, K.; Nakamura, E.; Ariga, K. Supramolecular Differentiation for Constructing Anisotropic Fullerene Nanostructures by Time-Programmed Control of Interfacial Growth. *ACS Nano* **2016**, *10*, 8796-8802.
- 12) Harano, K.; Minami, K.; Noiri, E.; Okamoto, K.; Nakamura, E. Protein-Coated Nanocapsules via Multilevel Surface Modification. Controlled Preparation and Microscopic Analysis at Nanometer Resolution. *Chem. Commun.* **2013**, *49*, 3525-3527.
- 13) Harano, K.; Gorgoll, R. M.; Nakamura, E. Binding of Aromatic Molecules in the Fullerene-Rich Interior of a Fullerene Bilayer Vesicle in Water. *Chem. Commun.* **2013**, *49*, 7629-7631.

Chapter 2

- 14) Harano, K.; Yamada, J.; Mizuno, S.; Nakamura, E. High-Density Display of Protein Ligands on Self-Assembled Capsules via Noncovalent Fluorous Interactions. *Chem. Asian J.* **2015**, *10*, 172–176.
- 15) Bragg, A. E.; Kanu, G. U.; Schwartz, B. J. Nanometer-Scale Phase Separation and Preferential Solvation in THF–Water Mixtures: Ultrafast Electron Hydration and Recombination Dynamics Following CTTS Excitation of I⁻. *J. Phys. Chem. Lett.* **2011**, *2*, 2797–2804.
- 16) Tabata, M.; Kumamoto, M.; Nishimoto, J. Chemical Properties of Water-Miscible Solvents Separated by Salting-out and Their Application to Solvent Extraction. *Anal. Sci.* **1994**, *10*, 383–388.
- 17) Przybilla, T.; Zubiri, B. A.; Beltran, A. M.; Butz, B.; Machoke, A. G. F.; Inayat, A.; Distaso, M.; Peukert, W.; Schwieger, W.; Spiecker, E. Transfer of Individual Micro- and Nanoparticles for High-Precision 3D Analysis Using 360° Electron Tomography. *Small Methods* **2018**, *2*, 1700276.
- 18) Grünwald, K.; Medalia, O.; Gross, A.; Steven, A. C.; Baumeister, W. Prospects of electron cryotomography to visualize macromolecular complexes inside cellular compartments: implications of crowding. *Biophys. Chem.* **2002**, *100*, 577–591.
- 19) Tian, Y.; Wang, T.; Liu, W.; Xin, H. L.; Li, H.; Ke, Y.; Shih, W. M.; Gang, O. Prescribed nanoparticle cluster architectures and low-dimensional arrays built using octahedral DNA origami frames. *Nat. Nanotechnol.* **2015**, *10*, 637–644.
- 20) Hayashida, M.; Malac, M. Practical electron tomography guide: Recent progress and future opportunities. *Micron.* **2016**, *91*, 49–74.
- 21) Jian, N.; Dowle, M.; Horniblow, R. D.; Tselepis, C.; Palmer, R. E. Morphology of the ferritin iron core by aberration corrected scanning transmission electron microscopy. *Nanotechnology*, **2016**, *27*, 46LT02
- 22) Earnshaw, W. C.; Hendrix, R. W.; King, J. Structural Studies of Bacteriophage Lambda Heads and Proheads by Small Angle X-ray Diffraction. *J. Mol. Biol.* **1979**, *134*, 575–594.
- 23) Lander, G. C.; Evilevitch, A.; Jeembaeva, M.; Potter, C. S.; Carragher, B.; Johnson, J. E. Bacteriophage Lambda Stabilization by Auxiliary Protein gpD: Timing, Location, and Mechanism of Attachment Determined by Cryo-EM. *Structure* **2008**, *16*, 1399–1406.
- 24) Pettersen, E. F.; Goddard, T. D.; Huang, C. C.; Meng, E. C.; Couch, G. S.; Croll, T. I.; Morris, J. H.; Ferrin, T. E. UCSF ChimeraX: Structure visualization for researchers, educators, and developers. *Protein Science* **2021**, *30*, 70–82.
- 25) Dale J. W.; Greenaway P. J. Preparation and Assay of Phage Lambda.; Walker J. M., Eds.; Nucleic Acids. Methods in Molecular Biology, 1984, *2*, 201–209.
- 26) Schindelin, J.; Arganda-Carreras, I.; Frise, E., Fiji: an open-source platform for biological-image analysis, *Nat. Methods* **2012**, *9*, 676–682.

Chapter 3.

第3章 本章については，5年以内に特許申請するため，非公開.

Chapter 6

Chapter 4.

第4章 本章については，5年以内に特許申請するため，非公開.

Chapter 6

Chapter 5.

第 5 章 本章については，5 年以内に特許申請するため，非公開.

Chapter 6

Chapter 6.

Conclusion and Perspectives

Chapter 6

Chapter 6

In the present study, I have demonstrated the application of supramolecular chemistry to the development of sample preparation methods in electron microscopy. I have prepared amorphous nano/microspheres and ultrathin films through self-assembly of organofullerene molecules modified their chemical properties by the introduction of various substituents. Since these materials are robust under atmospheric pressure and even under high vacuum, they were useful as supporting materials of EM research to modify the specimen location by the morphology of the supporting materials and protect the specimen structure from outer environments.

In chapter 2, the sample preparation method for structural analysis of nanomaterials with ET was described. While ET is a powerful method to reconstruct 3D data of target nanomaterials without averaging the numerous numbers of specimens and be suitable for capturing the inherent structure, image acquisition processes at various tilt angles in its procedure often suffer from decreasing the specimen contrast due to the increase of optical thickness of supporting materials. To tackle the issue, I presented the application of spherical supporting materials prepared from the molecular assembly of organofullerenes and succeeded to collect specimen images in constant contrast.

The method is simple that only requires the mixing of nanoparticle dispersions and organofullerene solutions in THF or DMF to prepare multiple-component nanospheres, therefore it is applicable for analysis of various specimens from inorganic nanoparticles to biomolecules including the virus. The key idea is an introduction of a rate control mechanism of nucleation and growth steps of molecular assembly. In this research, an equilibrium between neutral fullerene (**C_nH**) and its potassium salt (**C_nK**) in water was utilized and enable the formation of fullerene assemblies incorporating specimens from water/buffer. The developed system is expected to put a 360° tomography of various intended specimens into practice.

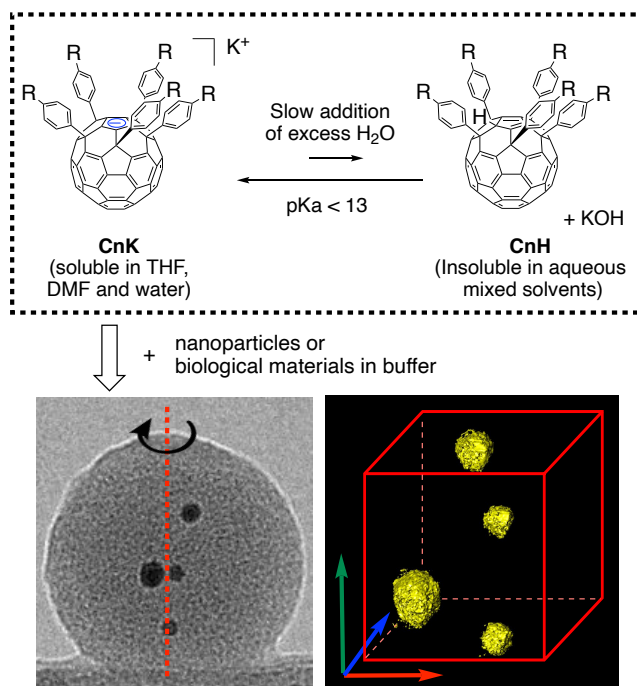


Figure 6.1. Preparation of self-assembled core-shell particles by utilizing an equilibrium of organofullerenes in water and structural analysis of incorporated specimens with ET.

The author anticipates that further chemical derivatization of organofullerenes and development of the hierarchical molecular assembly systems based on this work would contribute the structural analyses of wider specimens in EM research. Besides, some concepts of supra molecular chemistry described in this thesis would be applicable beyond the organofullerene skeleton, and the present study is expected to become a milestone of opening the new application field of molecular assembly systems.